**Marco António Bernardino Raimundo Costa**

Licenciado em Ciências da Engenharia Electrotécnica e de Computadores

# Calibration, Selection and Mosaicing of SMART-1 AMIE Images

Dissertação para obtenção do Grau de Mestre em Engenharia Electrotécnica e de Computadores

Orientador: José Manuel Fonseca, Professor Doutor, FCT/UNL
Co-orientador: André Damas Mora, Professor Doutor, FCT/UNL

Presidente: Prof. Doutor Yves Philippe Rybarczyk
Arguente: Mestre Miguel Alexandre Dias Almeida
Vogais Prof. Doutor José Manuel Matos Ribeiro da Fonseca
Prof. Doutor André Teixeira Bento Damas Mora

FACULDADE DE CIÊNCIAS E TECNOLOGIA
UNIVERSIDADE NOVA DE LISBOA

**Setembro de 2013**

**Calibration, selection and mosaicing of SMART-1 AMIE Images**

*À minha mãe e avós.*

# AKNOWLEDGEMENTS

Queria começar por agradecer à minha família. Não seria nada sem a minha imparável avó e a sua energia eterna, capaz de fazer incríveis sacrifícios por aqueles que ama. Assim como o meu avô, pela qual a idade parece não passar e mantém o mesmo grande coração e boa disposição que sempre conheci. Não me podia esquecer da minha tia e as suas perguntas incessantes que me fazem sempre sorrir. E claro, à minha mãe com seu apoio constante e incentivo, mesmo nos momentos mais difíceis. Para terminar, ainda à sempre pequenina Maria Luís e da sua constante motivação para seguir em frente, sem a qual a escrita desta tese teria sido bastante mais complicada. És um sol com esse sorriso.

Queria também agradecer a todos os professores que nestes anos contribuíram para a minha aprendizagem, mas especialmente aos professores José Manuel Fonseca e André Mora. Foram como uns mentores neste último ano. A vossa incrível disponibilidade, interesse e rigor por tudo o que vos rodeia fez-me desejar encontrar mais pessoas como vós neste ciclo profissional que agora se inicia. Um sincero obrigado.

Durante estes muitos amigos e colegas deixaram a sua marca. Ao Luís Pedro pelas muitas horas a debater ideias e contribuição para este e muitos outros trabalhos. Ao Rui que nunca me deixou esquecer que continua a haver vida fora da faculdade. Ao Pedro pela constante boa disposição e good vibe. Ao Tiago pelo foco que imprime a tudo o que se envolve. A toda a Malta pela incessante conversa sobre filmes e séries que parece nunca irá parar. E a muitos outros que não disse o nome mas estão sempre presentes.

A todos, Muito Obrigado.

# ABSTRACT

Small Missions for Advanced Research in Technology (SMART-1), represented European Space Agency (ESA) first mission to the moon. It fulfilled the goal of improving the scientific knowledge of earth's natural satellite, while testing new technologies that had never been used in space exploration. Among the on board instruments of SMART-1 was the Advanced Moon micro-Imager Experiment (AMIE). It was an imaging equipment whose mission was to map the lunar surface providing state-of-the-art resolution. Containing six filters inside its visual scope AMIE allowed the study of the surface composition by multispectral imaging.

This thesis aims at building a set of maps covering approximately all the Moon surface as it was mapped by the SMART-1 spacecraft, using the 31945 images captured by the AMIE instrument. During the Earth escape phase the instrument's CCD was damaged by radiation, causing the accumulation of dark current and invalidating the laboratorial image calibration algorithm. The acquired dataset also suffered from scattered light that got beneath the CCD filters and reduced their contrast. In order to overcome this problem, a new calibration procedure was developed using the in-flight collected data and theoretical models, as well as a method to compensate for the reduced contrast in the filters.

For building the lunar maps, the images were individually analysed and classified accordingly to their visual quality and grouped by their illumination conditions, allowing the creation of visually balanced maps. Image mosaicing and projection techniques were used to compensate the geometrical distortions and compose the calibrated images into a set of 88 maps of the Moon. Increasing the flexibility of the process, a comprehensive tool that allows the edition of the images in the mosaiced maps, as well as brightness and contrast correction and adjustment is also presented.

**Keywords:** Space exploration, Lunar mapping, Moon atlas, Calibration, Image mosaicing, Image enhancement.

# RESUMO

A SMART-1, *Small Missionsfor Advanced Research in Technology*, representou a primeira missão da *European Space Agency* à Lua; cumprindo o objectivo de melhorar o conhecimento científico do satélite natural da Terra, ao mesmo tempo que testava novas tecnologias nunca antes utilizadas na exploração espacial. Entre os seus instrumentos encontrava-se o *Advanced Moon micro-Imager Experiment* (AMIE), um equipamento de captura de imagem que mapeou a superfície lunar com, na altura, resolução topo de gama. Equipado com seis filtros no seu campo visual, o AMIE permitiu ainda o estudo da composição da sua superfície.

Este trabalho tem como objectivo a construção de um atlas da Lua como foi mapeado pela SMART-1, utilizando para isso as 31945 imagens capturadas pelo instrumento AMIE. Durante a fase de fuga da Terra o CCD do equipamento foi danificado pela radiação, levando à acumulação de *dark current* e invalidando o algoritmo de calibração laboratorial das imagens. O *dataset* foi também afectado por deflecção de luz entre o CCD e os filtros, reduzindo o seu contraste. Um novo procedimento de calibração foi criado utilizando os dados adquiridos durante o voo e modelos teóricos, assim como um método de compensação para a redução de contraste nos filtros.

Para a criação dos mapas lunares, as imagens foram analisadas individualmente, classificadas de acordo com a sua qualidade visual e agrupadas segundo as suas condições de iluminação, permitindo assim a melhor equilíbrio visual possível nos mapas. Mosaico de imagens e técnicas de projecção foram utilizadas para compensar as distorções geométricas e juntar as imagens calibradas num conjunto de 88 mapas Lunares. Aumentando a flexibilidade do processo, uma ferramenta completa que permite a edição das imagens nos mapas construídos, assim como a correcção e ajuste do contraste e brilho, é também apresentada.

**Palavras Chave:** Exploração espacial, Mapeamento lunar, Atlas da Lua, Calibração, Mosaico de imagens, Processamento de imagem.

# INDEX

# LIST OF FIGURES

# LIST OF TABLES

# LIST OF ACRONYMS

# 1 INTRODUCTION

Mankind interest in space is present since the dawn of time. The blue of dark sky was always a giant origin of curiosity on Man's soul that not even the evolution of knowledge and technology could erase. However, only on the 20th century there was finally a chance to explore it.

That chance came from war and the technological advances it brought. Until the 2nd World War rockets weren't powerful enough to project any object into orbit. It only changed when the desire to overpower the enemy with bigger weapons at longer distances struck. Fortunately those advances found its way to different uses such as space exploration.

One of those missions propelled by pursuit of knowledge was the European Space Agency's (ESA) Small Missions for Advanced Research in Technology-1 (SMART-1). The focus this thesis is the calibration, selection and mosaicing of the images captured by one of its instruments, the Advanced Moon Micro-Imager Experimenter (AMIE), with the intent to build a lunar atlas.

Below on this chapter the SMART-1 mission is described together with the detailed characteristics of the AMIE instrument, as well as the dataset issues and the thesis objectives. On chapter 2 a review of previous missions and relevance to the lunar mapping and atlas is presented. The methods applied to achieve the thesis objectives are detailed in the chapter 3 and finally on chapter 4 the discussion of results obtained and conclusion is presented.

## 1.1 SMART-1 MISSION

Launched on 27th September 2003 from the Guiana Space Centre in Kourou, French Guiana, SMART-1 was the first mission of the European Space Agency to the Moon. It was also the first and the last of the SMART mission series that was repurposed and renamed. The mission was planned to test new technologies for future missions and was part of the ESA strategy to build smaller low-cost spacecrafts [1].

It reached lunar capture on 15th November 2004 and science orbit of 400-3000Km on 15th March 2005. The mission nominal time was six months plus a one year extension in lunar science orbit [2]. The mission ended on the 3rd September 2006 on a controlled crash against the lunar surface in the Lacus Excellentiae region at a speed of 2 km/s and very shallow angle of incidence (~1°) [3].

Figure 1.1 - The ESA SMART-1 spacecraft

The mission had both technical and scientific objectives, performing ten investigations based on three remote sensing instruments. Among the technical was performing a Laserlink experiment (the detection of a laser beam emitted by ESA/Tenerife ground station), flight demonstration of new technologies and on-board autonomy navigation. The science objectives were to image the lunar South Pole, permanent shadow areas (ice deposit), eternal light (crater rims), ancient lunar non-mare volcanism, local spectrophotometry as well as the physical state of the lunar surface and to map high altitude regions (the south) mainly at the far side (South Pole Aitken basin).

### 1.1.1 Instruments and Technology

After being launched into orbit on board of an Ariane-5 rocket with other two satellites, it set a record by being the maiden mission to leave Earth orbit using only solar power, as well as setting the lowest fuel consumption per km for any Moon mission (but also the longest, 13 months) [4].
For that it used the Solar Electric Primary Propulsion (SEPP), an Hall Effect thruster that for its lightweight and small consumption is ideal for long-duration deep-space missions [5] [6]. As an addition, the SEPP by operating with a noble gas such as Xenon, that is known for good storability, also allows costs saving in safety procedures during ground operations.

The SMART-1 mission was also the first to use the Ka band for downlinking scientific data, latter used by other missions as the Mars Reconnaissance Orbiter and the Kepler space telescope. This system adopted the name Ka band TT&C (telemetry, tracking and control) Experiment (KaTE).

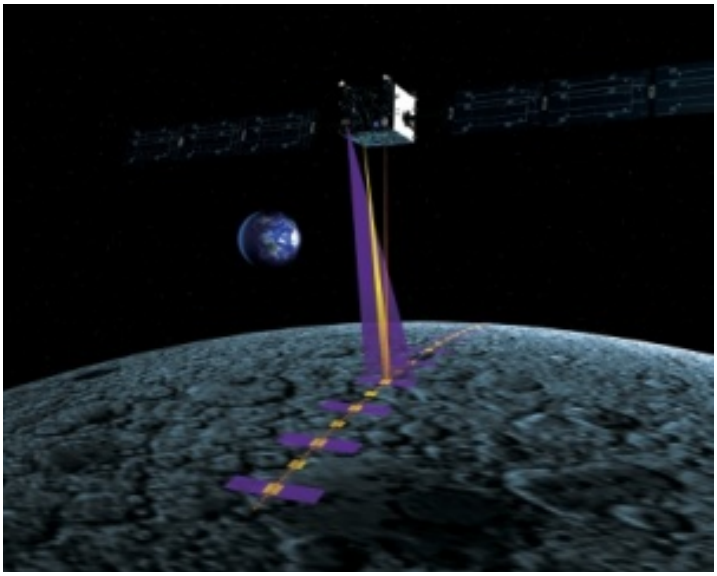

Figure 1.2 - Comparison between the swaths of the SMART-1 remote sensing instruments in lunar orbit: D-CIXS (32 · 12°), AMIE (5 · 5° or 2.5 · 1.25° colour frames) and SIR (400 point spectral continuous mapping). [2]

To accomplish its scientific goals the spacecraft was equipped with three remote sensing instruments for lunar study.
The Advanced Moon Micro-Imager Experimenter (AMIE) was an ultra-compact lightweight imaging system capable of capturing images in the visible and near infrared, which will be the basis of this thesis work and described in detail in chapter 1.1.1.1. The AMIE instrument was also used to perform the laserlink experiment that aimed at testing the feasibility of optical communications at long distances, as is the case of Earth to Moon. The interest of this experiment lies in the potential for greater data transfers during space missions.

The SMART-1 Infrared Spectrometer (SIR) was an infrared spectrometer, operating in the 0.9 to 2.6 μm wavelength range, to separate the signature of pyroxene and olivine. Olivine is considered to be

the common element of Moon's mantle and yet was poorly constrain in contemporary models. The study of the element distribution among the crust and surface would allow a perspective on the crustal differentiation and evolution [7]. As part of this study one of the main focuses was the South Pole Aitkin basin as it could have been dug through to expose materials from the Moon's mantle.

The third equipment for lunar study was the Demonstration of a Compact Imaging X-ray Spectrometer (D-CIXS) which mapped the lunar surface for X-ray fluorescence (XRF) in the 0.5 to 10 keV range. This allowed for the bulk estimation of the elements Al, Mg and Si which has a direct bearing on the Giant Impact Theory of the Moon originating from the Earth. As well as the spectrometer the D-CIXS also included a Solar X-ray Monitor (XSM) which measured the Sun's X-rays and to serve as a calibration for the D-CIXS data.
This study was the first XRF measurement since Apollo missions 15 and 16, and far more extensive as those only covered 9% of the Moon's surface and were limited to the equatorial regions. More importantly was the first to give absolute elemental abundances instead of just elemental ratios.

Three other instruments were carried for navigation as well as for technological study, the Electric Propulsion Diagnostic Package (EPDP), Spacecraft Potential, Electron and Dust Experiment (SPEDE) and Radio Science Investigation with SMART-1 (RSIS). EPDP monitored the propulsion system, providing feedback for future solar electric engine designs. SPEDE was responsible for measuring the solar wind and besides the navigation purposes it was also used to perform studies while in lunar orbit. Finally the RSIS used AMIE's high resolution and KATE to study the Moon's libration with accurate orbit determination.

#### 1.1.1.1 ADVANCED MOON MICRO-IMAGER EXPERIMENT (AMIE)

The Advanced Moon micro-Imager Experiment (AMIE) embedded on the SMART-1 spacecraft was an electronic miniaturised micro-camera and micro-processor built with the primary goal of imaging the lunar surface. The primary objectives were to imaging the South Pole permanent shadow areas, eternal light, ancient lunar non-mare volcanism, perform local spectrophotometry and physical state of the lunar surface and to map high latitudes regions (mainly at far side, e.g. the South Pole Aitken basin).

The imaging system was divided into two units, a camera unit and a dedicated electronics unit [8].
The camera was composed by a 5,3°x5,3° field of view (FOV) tele-objective and a 1024x1024 charge-coupled device (CCD) sensor. At the spacecraft apolune (at 3000km altitude from the Moon) the FOV produced an image resolution of 270m/pixel and at its perilune (at 300km of altitude over the South Pole) 27m/pixel image.
The sensor was divided into three spectral filtered areas of 750, 915 and 960nm, a smaller filtered area of 847nm also used for the Laserlink experiment and a 512x512 area without filtering, as is presented in Figure 1.3. While the 750 and 915nm filters were narrow band filters centred at the mentioned wavelengths and with a respective width of 10 and 30 nm, the 960nm filter was a high pass filter with steep transmission edge.

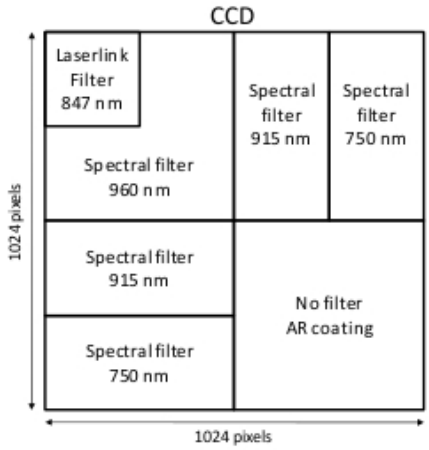


Figure 1.3 - Scheme of CCD field of AMIE/SMART-1 camera.

The electronic unit was responsible for the data control and power management of the camera. A Micro-DPU controlled the data processing and compression, image data storage into the data mass buffer, communication with the S/C and adaptation of the S/C supply voltage to the levels required by its electronics and the camera [8].

By capturing the same region with 3 different spectral bands the sensing unit allowed the discrimination of mafic materials (such as the pyroxenes and olivines that compose the mare on highland regions) by the $Fe^{2+}$ absorption feature at 0.95μm. Also the imaging allowed the study of solar winds and micro-meteorites effect on the Moon's surface as part of its maturation process.

On the 21st September 2010 the complete ESA's SMART-1 data archives were released to the scientific community and among them were 31945 CCD full frames captured by AMIE instrument [4] [9] [10] [11] [12] [13] [14]. This dataset, the objective of this thesis, provides high-resolution mapping of the lunar surface, especially at the south polar area.
Since in the released AMIE dataset each captured image of the CCD is divided into several individual files, according to the filter it belongs, from now on the complete image will be referred to as a *full frame*. The individual filters images will simply be referred as frames or individual frames.

## 1.2 AMIE DATASET ISSUES

Upon individually analysing the AMIE captured images several issues were discovered to have affected the dataset:

- The Van Allen radiation belts are at least two radiation zones of energetic charged particles around planet Earth at a distance between 650 and 650 000 km of altitude. [15] During Earth escape phase the SMART-1 spacecraft crossed the belts numerous times and was subjected to high doses of radiation which caused an increase in dark current accumulation on the CCD. This fact yielded the dark current compensation and camera flat field images, acquired during laboratory ground tests, inadequate to calibrate the mapping done during lunar an extended phase of the mission.

- When the instrument was switched on without capturing any image a considerable amount of dark current accumulated near the readout area, saturating that area of the captured frames.

- Many images suffer from a vertical stripes pattern with 8 pixel spacing and variable positioning. This effect is more noticeable on images with low light levels.

- A relatively large number of images presented corrupted blocks of pixels, where the pixels in that area present no discernable features while the remaining of the captured full frame has good quality.

- The filtered areas of the CCD full frame present a much lower contrast in comparison to the unfiltered portion. This is due to scattered light that got beneath the filters panel from the border with the unfiltered area.

## 1.3 OBJECTIVES

The objective of this thesis is to achieve visually balanced and attractive lunar maps using the SMART-1 AMIE dataset images to be published as a SMART1 Moon Atlas.

With that goal in mind each issue mentioned in chapter 1.2 will be studied and processed to improve the calibration results and maximize images quality.

As the artificial satellite orbits around the Moon it also varies its position relatively to the Sun changing lighting conditions. Therefore, the images in the dataset present different illumination conditions that affect their quality. An adequate selection of the images to be projected into the maps will then have a severe effect on map's quality and balance and should be addressed.

Earlier attempts to mosaic SMART-1 images showed that some full frame images present very different data values resulting in over brighten areas in the mosaiced map. Despite the images' good quality the model brightness scaling could not compensate this effect and a solution should be found to allow the usage of these images.

Finally, to ease the map mosaicing process a tool should be created in order to allow a better control over the process and to make any possible correction or adjustment that the automated process could not achieve.

# 2 STATE OF THE ART REVIEW

In this chapter a review of past space missions with Moon mapping objectives is made. Presented in chronological order, each of them represented not only a mark in history but also high scientific relevance at contemporary or current time. While some missions like Luna 3 have been surpassed by technologically more advanced missions, others as the Clementine mission are still being used as a reference in moon mapping.

The information presented in this review includes among others the technological equipment used and the mapping coverage, quality and resolution. These are key elements in the construction of an atlas. Below, on chapter 2.1 an individual review of each of the mapping missions with the mentioned relevant information is made.

## 2.1 INDIVIDUAL REVIEW

Here an extensive individual review of each of the most relevant lunar mapping missions or projects is presented in a chronological mission launch order.

### 2.1.1 Luna 3

The Luna 3 mission was a milestone in space exploration allowing mankind to see for the first time the moon's far side. Using a complex imaging system to capture and relay images back to earth it provided a total of 29 images that might be considered low quality by today's standards, but still a feat at the time.

The spacecraft, built by the Union of Soviet Socialist Republics (USSR), was launched on a Luna 8K72 rocket on October 4$^{th}$ of 1959 and three days later took the first picture, the one showed in Figure 2.1.
The imaging system consisted of a dual-lens camera, with a 500mm f/9.5 aperture and a 200mm f/5.6 aperture, as well as an automatic film processing unit, a scanner and a radio system. This system allowed the film to be converted into a frequency-modulated analog video format that could be relayed back to Earth. [16]

The 29 photographs captured covered 70% of the far side of the moon and were taken during a 40 minutes span. The first image was captured when the spacecraft was at a distance of 65567 km from the moon's centre, and the last at 68785 km. During the process the telemetry was switched off to save power and no altitude information is available. [17]
The resulting pictures were very noisy and low resolution, but many features could still be recognized. It showed a very different terrain from the near side, very mountainous with only two dark regions.

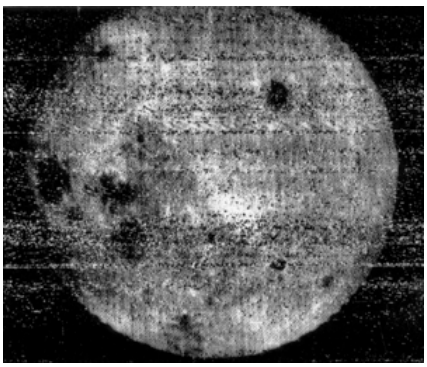

Figure 2.1 - First captured image of the moon's far side

In 1959 a book containing 28 out of the 29 Luna 3 images, 4 outline maps and lunar features description was assembled by the scientists of the main research centres in charge of analysing and processing the images retrieved by the mission. Named *Atlas of the Far Side of the Moon* [18] it gained popularity as it was the only published book containing images of the hidden side of Earth's natural satellite for nearly 6 years.

### 2.1.2 LUNAR ORBITER

The Lunar Orbiter project consisted of five identical unmanned spacecraft launched between 1966 and 1967. These were built with the primary goal of exploring for possible landing sites for the future United States' (US) Apollo program. However, by the end of the third mission most of their objectives had been met and part of the remaining missions' time was open for scientific exploration. [19]

Similar to other contemporary and previous mapping missions, these were equipped with a dual-lens camera, a film processing unit, readout scanner and a film handling apparatus. The type of equipment and setup was kept the same throughout the missions.

The lenses consisted of an 80mm, used for medium resolution, and a 610mm, used of high resolution shots. These were prepared so that shots taken from with the high resolution camera would coincide with the centre of the medium resolution frames. When shooting, the pictures of the different lenses were captured into adjacent areas of the same 70mm film supply, which was kept moving during exposure to compensate for the spacecraft's velocity [20].

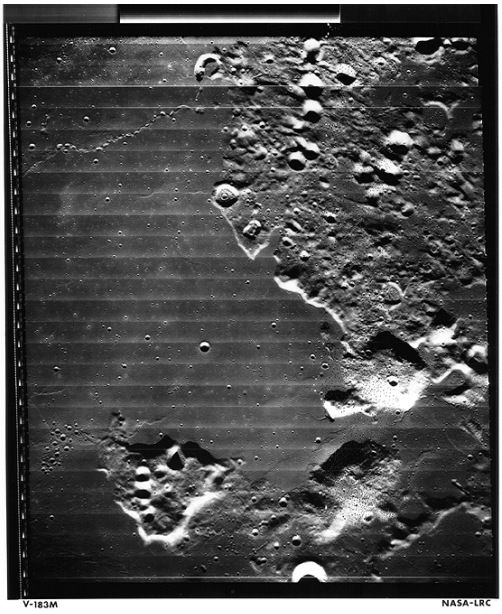


Figure 2.2- Craters in northern Oceanus Procellarum on the Moon taken by Lunar Orbiter 5

The Lunar Orbiter 1, 2 and 3 missions covered 22 possible landing sites near the equatorial area, taking pictures at low inclination and low altitude orbits for geological and topography study [19]. In addition they also took the opportunity to study the spacecraft's trajectory, to improve the lunar gravity definition, and measurements of micrometeorites and lunar radiation flux for performance improvement.

Despite maintaining its secondary objectives of gravitational field and environmental study, the Lunar Orbiter 4 main objective was the extensive survey of lunar topography. Its cameras photographed the surface during 29 successive orbits in 15 days, covering approximately 99% of near side and a large portion of the far side. The images captured provided at least 10 times more detail than the previously captured from earth-based telescopes.

The final Lunar Orbiter mission was meant to complement the previous missions, taking additional high quality images of possible landing sites for the future missions and scientifically interesting sites at highly inclined orbits (85 degrees, as used in mission 4). It focused primarily on 68 photo sites during its orbits, 45 on the near side and 23 on the far side, with a resolution between 20 meters (for medium resolution frames) and 2 meters (for high resolution). In Figure 2.2, despite visible lines created during readout, is noticeable the good quality of the images captured by the last spacecraft of the Lunar Orbiter missions.

By the end of the last Lunar Orbiter mission 99% of the entire moon's surface had been mapped with a resolution of 60 meters or better. The summary of captured images and flight information of the entire Lunar Orbiter Project is presented in Table 2.1.

Table 2.1 - Detailed Information on Lunar Orbiters and Images collected [21]

| **Photographic Parameters** | | **Lunar Orbiter 1** | **Lunar Orbiter 2** | **Lunar Orbiter 3** | **Lunar Orbiter 4** | **Lunar Orbiter 5** |
|---|---|---|---|---|---|---|
| Launch Date | | 10 Aug 1966 | 10 Nov 1966 | 05 Feb 1967 | 04 May 1967 | 01 Aug 1967 |
| Periselene (km) | | 40.5 | 41 | 44 | 2668 | 97 |
| Aposelene (km) | | 1857 | 1871 | 1847 | 6151 | 6092 |
| Inclination (deg) | | 12 | 12 | 21 | 85.5 | 85 |
| Period (h) | | 3.5 | 3.5 | 3.5 | 12 | 8.5,3.0 |
| Impact date | | 29 Oct 1966 | 11 Oct 1967 | 10 Oct 1967 | 31 Oct 1967 | 31-Jan-68 |
| Impact coordinates | | 7 N, 161 E | 3 N, 119.1 E | 14.32 N, 92.7 W | ??, 22-30 W | 2.79 S, 83 W |
| Acquisition dates | | 18-29 Aug 1966 | 18-25 Nov 1966 | 15-23 Feb 1967 | 11-26 May 1967 | 06-18 Aug 1967 |
| Quantity of frames | *High resolution* | 42 | 609 | 477 | 419 | 633 |
| | *Medium resolution* | 187 | 208 | 149 | 127 | 211 |
| Altitude range for photography (km) | | 44 - 1581 | 41 - 1519 | 44 - 1463 | 2668 - 6151 | 97 - 5758 |
| Highest resolution | *Periselene (m)* | 8 | 1 | 1 | 58 | 2 |
| | *Aposelene (m)* | 275 | 33 | 32 | 134 | 125 |
| Framelet width at periselene (m) | *High resolution* | 200 | 170 | 185 | 11350 | 420 |
| | *Medium resolution* | 1500 | 1300 | 1400 | 85100 | 3200 |

In 1971 David Bowker and Kenrick Hughes of the National Aeronautics and Space Administration's (NASA) Langley Research Center published the *Lunar Orbiter photographic atlas of the Moon* [22]. In this book they assembled 675 plates of the Lunar Orbiter missions into a detailed atlas with annotations on the named moon's features. It included plates both from the near and the far side and was mostly based on the fourth mission survey.
The *Lunar Orbiter photographic atlas of the Moon* became a reference for lunar topography for its high quality pictures and detailed information. Today due to its rarity a used copy is highly valued, being nowadays found for sale at prices above 400 US dollars.

### 2.1.3 CLEMENTINE

Built by the joint forces of NASA and the Ballistic Missile Defense Organization of the US Department of Defense, the Clementine mission consisted of an unmanned spacecraft launched from Earth on the 25$^{th}$ of January of 1994. This mission came as a result of the increasing need for lunar mapping using

a variety of sensing techniques, consistently expressed in the previous 20 years [23]. Therefore, its science objectives were defined as to obtain topographic imaging, altimetry data and multispectral imaging of the lunar surface. The Clementine mission was the first to acquire a digital image data set of the moon.

The spacecraft was equipped with four cameras: an ultraviolet/visible camera (UVVIS), a long-wave infrared camera (LWIR), a high resolution camera (HIRES) equipped with a laser ranging system (LIDAR) and a near-infrared camera (NIR) [24]. As an addition it also had two star-tracker cameras used essentially for altitude determination, but that could also be used as wide-field cameras for scientific or other operational purposes.
The UVVIS camera was a CCD imager with a six filter wheel, with filters centred from 415 up to 1000nm and a broad-band filter covering from 400 to 950nm. The NIR also had a six filter wheel but with filters ranging from 1100 up to 2780nm. The LWIR had a bandwidth from 8000 to 9500nm and the HIRES camera a broadband filter from 400 to 800nm, as well as four other filters centred from 415nm up to 750nm. In addition to the mapping cameras it also carried a charged-particle telescope, which had the objective of studying the solar and magnetospheric energetic-particle environment.

Arriving at Earth's natural satellite on 19 of February of 1994 it remained operational during 71 days with a 5-hour elliptical polar orbit. During this period took 620 000 high resolution and 320 000 mid-infrared thermal images to an approximated total of 2.8 million images, as well as mapped the lunar topography with its laser-ranging system. It covered 38 million square kilometres mapping the moon in 11 visible and infrared colours with an average resolution of about 200 meters per pixel.

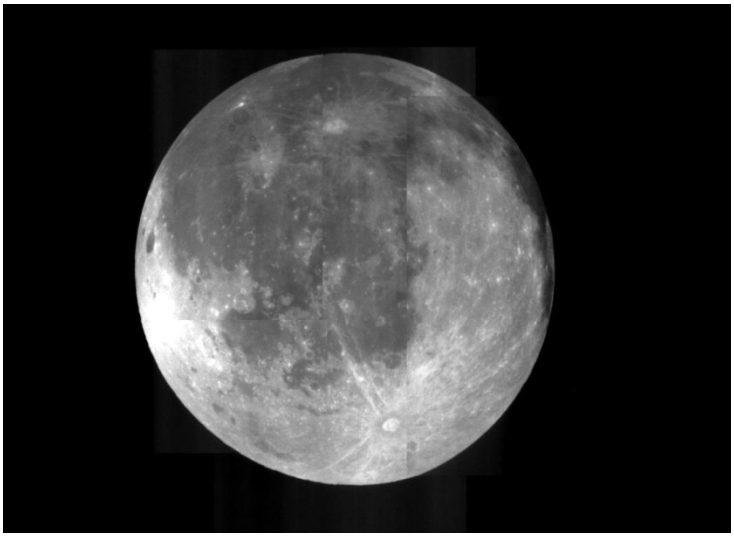

Figure 2.3 - Mosaic of the near side of the moon as taken by the Clementine star trackers.

Besides the mapping objectives, it also provided with more accurate spacecraft position tracking data, used to improve the lunar gravitational field model. Despite the already provided data from the Apollo and Lunar Orbiter earlier missions these were either only restricted to equatorial regions or the tracking resolution at the time was only enough to provide a fairly coarse potential field model. [25]

Among the relevant scientific discoveries was the relevance of the South Pole-Aitken basin. Being the largest basin on the Moon, with more than 2500 km in diameter and 13 km of depth, it was found that has maintained much of its original relief [25]. Not only was in an amazing preservation state but the compositional data showed that its floor has the largest composition anomaly on the far side, having significantly higher quantities of iron and titanium contents than any other location.

Currently the images and data collected during the Clementine mission are of extreme relevance, being used in broad areas of application. These include not only scientific but also widespread atlas applications such as Google Moon, which bases its entire visible layer upon the Clementine image mapping after has been prepared by the United States Geological Survey (USGS). [26]

### 2.1.4 LUNAR PROSPECTOR

The Lunar Prospector spacecraft was a complementary low-budget mission of the previous Clementine. While the later was equipped mostly with imaging cameras the Lunar Prospector equipment was essentially composed by spectrometers to study the Moon's composition, as well as equipment to analyse the gravity and magnetic field [27]. Launched on 7 January 1998 by an Athena 2 rocket it reached Moon's orbit 105 hours later, maintaining operations for 570 days.

Aboard the spacecraft were a Gamma Ray Spectrometer (GRS), a Neutron Spectrometer (NS), a Magnetometer (MAG), an Electron Reflectometer (ER), an Alpha Particle Spectrometer (APS), and a Doppler Gravity Experiment (DGE) [28].

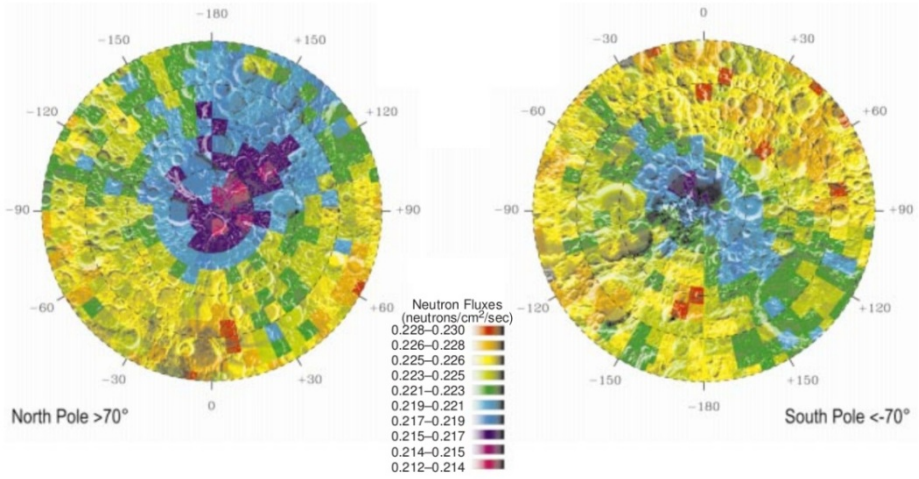


Figure 2.4 - Epithermal counting rates poleward of ±70º

Among the most relevant scientific studies was the existence of water on the Moon's polar regions, subject which had once more been raised upon the data collected from Clementine mission. Maps of epithermal and fast-neutron fluxes measured by the Lunar Prospector were used to search for deposits of hydrogen in both poles. [29]

The data was consistent with water ice deposits buried beneath 40 cm of dry regolith in an estimated area of 1850 km² at both poles, as shown by epithermal counting rates in Figure 2.4. In an attempt to further confirm this, a crater near the South Pole was chosen as the controlled crash site for the end of the mission while was being observed by Earth-based observatories and the Hubble Space Telescope. [30] Although a successful crash was achieved the data collected showed observable water signature.

## 2.2 SYNTHESIS

As mentioned before, the URSS Luna 3 space mission was the first to photograph the Moon's far side. Launched in 1959 at the beginning of the space race, the technology it carried was only capable of producing a small number of blurry low resolution images, covering 70% of the Moon's far side. This did not stop them from being assembled and used as part of the *Atlas of the Far Side of the Moon* [18].

Seven years later a project spanning for five missions named Lunar Orbiter was launched, with the primary objective of mapping the lunar surface for possible landing locations for the upcoming Apollo program. The success of the first missions allowed the opening of mission time for scientific exploration. By the end of the project the Lunar Orbiters had map 99% of the lunar surface with a resolution of 60m or better. In 1971 David Bowker and Kenrick Hughes published the *Lunar Orbiter*

*photographic atlas of the Moon* [22] with detailed annotations by assembling 671 plates of the Lunar Orbiter dataset.

The next extensive lunar mapping occurred only 27 years later in 1994. The Clementine mission included several cameras in the ultraviolet, visible and infrared spectrum of light, high resolution camera, laser raging system along with equipment for other scientific studies. It captured approximately 2.8 million images and the mapping achieved is currently still used as a reference for other space missions (the SMART-1 included). The captured visible/ultraviolet images are broadly used on Moon atlas inclusively the most currently widely spread digital lunar atlas, the Google Moon.

Launched in 1998 the Lunar Prospector was a low-budget mission complementary to the Clementine mission. Carrying mostly spectrometers it studied Moon's composition as well as its magnetic and gravitational field. Among its most relevant studies was the detection of water deposits, something that the data collected was consistent with, especially on the polar areas.

# 3 METHODOLOGY

In this chapter the methods applied with the goal of achieving the best possible mosaiced lunar maps, as well as the objectives defined in chapter 1.3, are described in detail. The information is presented in the order in which the process should be executed, following the flowchart in Figure 3.1. Its practical implementation was achieved using the mathematical computational environment MATLAB® [31].


Figure 3.1 - AMIE map construction process

It begins by improving the AMIE dataset full frames by calibrating each one (chapter 3.1). This step removes the effect of dark current, electronic noise, pixel-by-pixel sensitivity differences and scattered light that penetrated between the filters and CCD. During the calibration each full frame is also checked for corrupted blocks of pixels and each full frame's brightness is scaled for map illumination balance.

In chapter 3.2 the map organization of the AMIE Moon Atlas is detailed. Besides the map division is also described the map area coverage, the type of projection used and the dataset coverage on each of the maps. It is also discussed the information required for the full frames geometric computation and its pointing accuracy.

The map mosaicing in chapter 3.3 includes the projection methods applied, the full frames classification according to their visual quality and their organization order for projection. Finally the Map Builder is the tool responsible for handling the execution process of the methods described in the previous chapters, editing the mosaiced maps and performing the final needed brightness and contrast adjustments (chapter 3.4).

## 3.1 CALIBRATION

The calibration process of the AMIE CCD full frames aims at achieving brightness and contrast balanced images while reducing the noise. To do so the standard calibration of the camera must be done. That includes the removal of the dark current effects (chapter 3.1.1) as well as the removal of sensitivity differences between pixels, in the process referred to as *Flat Fielding* (chapter 3.1.3).

As an addition several other processes had to be introduced to address the dataset issues detected in chapter1.2. The Vertical Stripes Correction of chapter 3.1.2 applies a weighted line median filter as a method to remove the stripes pattern present in some full frames at low light, without compromising image quality. Chapter 3.1.5 applies a detection method to mark and exclude the 128 by 128 corrupted blocks of pixels from further processing and mosaicing while maintaining the rest of the uncorrupted full frame. The lower contrast in the filtered areas of the full frame caused by the scattered light is addressed in chapter 3.1.6 in a more direct to the problem approach that includes contrast enhancement.

Also included in the process is the Model Brightness Scaling of chapter 3.1.4, where each image brightness is scaled according to its illumination conditions using the Hapke model to compensate for their variability. The goal is to have the brightness of all images of the map balanced for the mosaicing process. Although not part of the calibration, the scaling is included as it must be applied before the 128 Corrupted Blocks Detection and the Scattered Light Correction.

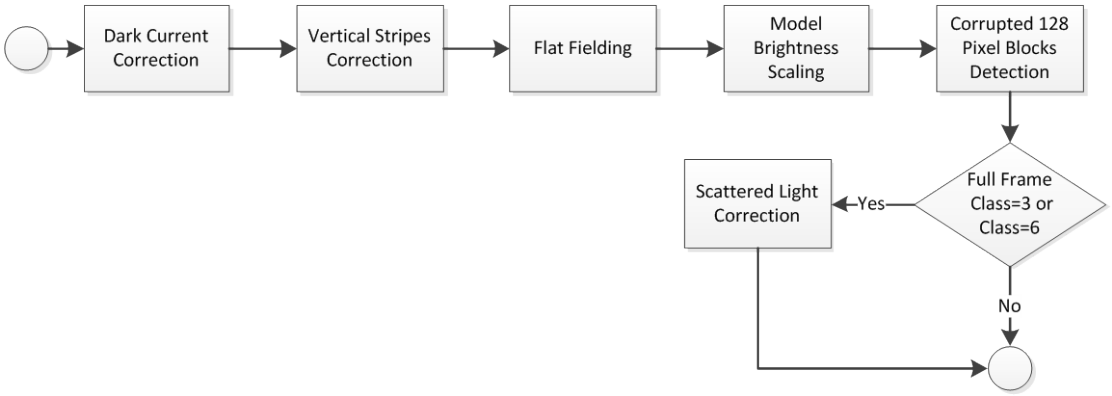


Figure 3.2 - Calibration process

The complete calibration process is described in Figure 3.2 with the different blocks presented according to its execution order. The Scattered Light Correction is only applied in the cases where the full frame has been classified with class 3 or class 6, those classes that mark both filtered and unfiltered areas of the full frame as usable. The AMIE full frame classification is described in chapter 3.3.1.1.

### 3.1.1 DARK CORRECTION

Dark current builds up in CCD sensors whether they are exposed to radiance or not, producing noise with random pixel accumulation that affects the quality of the acquired frames. This is caused by thermally created electrons and holes that build up in the pixels, having a direct relation with CCD temperature and exposure time. To remove this pattern a dark image is used (or a combination of dark images) and bias image, which is an image with no exposure time to compensate for the noise created by the CCD electronics. Therefore, the $D$ data number for an acquired pixel will be defined by equation (3.1)

$$D = d_0 + B \cdot f(T) + S \cdot f(T) \cdot t_e + C \cdot I \cdot t_e \tag{3.1}$$

Where $d_0$ is a fixed data number offset (8 in the SMART-1 AMIE case), $B$ the bias built up during readout, $f(T)$ the function describing the temperature dependence, $S$ the dark current during exposure, $t_e$ the exposure time, $C$ the radiance conversion factor and $I$ the incoming radiance. The temperature function and exposure time are pixel independent, the remaining are not.

In order to assess the dark current contribution a frame with incoming radiance $I = 0$ is needed, which results in the simplified equation (3.2). The frame is then subtracted to the original $D$ data numbers to obtain the corrected frame (equation (3.3)).

$$D_{Dark} = d_0 + (B + S \cdot t_e) \cdot f(T) \tag{3.2}$$

$$D_{Corr} = D - D_{Dark} \tag{3.3}$$

During Earth's escape phase the CCD sensor suffered an increased accumulation of dark current due to numerous radiation belt crossings, leaving the previously laboratory acquired dark frames inadequate to perform the correction. A new set of dark frames were acquired from in-flight data of dark sky observations during the lunar and extended phase of the mission. [32] To reduce the effect of noise and possible pixel errors a total of 154 dark sky images were used. To remove the temperature contribution an estimation was made using equations (3.4) and (3.5).

$$f(t) = \left(\frac{T}{T_0}\right)^{\frac{3}{2}} \cdot exp\left(\frac{E_g(T_0)}{2.k.T_0} - \frac{E_g(T)}{2.k.T}\right) \tag{3.4}$$

$$E_g(T) = 1.11557 - \frac{7.021\,.\,10^{-4}.T^2}{1108K + T} \tag{3.5}$$

Where $T_0$ is a reference temperature (which was chosen to be $T_0 = 273.15K$) and $k$ the Boltzmann constant ($k = 8.6171 \cdot 10^{-5} eV/K$).

After removing the offset $d_0$ and temperature $f(t)$ the dark frames have only the contribution of the bias $B$, which is independent of exposure time, and the dark current slope $S$ (equation (3.6)). A frame with null exposure time is not achievable, but the same result can be obtained by interpolating two or more full frames (on this case the 154 chosen dark sky images) to an exposure time $t_e = 0$ on each pixel. By doing this a bias plus offset ($d_0 + B$) estimation can be retrieved, as well as the slope $S$.
Having all the elements needed to obtain the dark frame $D_{Dark}$, the correction is then simply done using equation (3.3) as previously mentioned.

$$B(x,y) + S(x,y) \cdot t_e = \frac{\mathrm{D}(x,y,k) - d_0}{f(T)} \tag{3.6}$$

When the instrument was switched on without capturing any image a considerable amount of dark current accumulated near the readout area, saturating that area of the frames. This charge was swept away whenever a new frame was captured. When this problem was detected a procedure of capturing a frame without downloading it was implemented by ESA's operators, but still some of the dark frames used to estimate the dark correction suffer from this problem, propagating it to the corrected images. This effect is clearly visible at the top of Figure 3.5.

To avoid extending the effect to the AMIE map mosaics, the top 128 pixels of each full frame are removed before the scattered light compensation and are not included in the further processing or mosaicing.

### 3.1.2 VERTICAL STRIPES

As can be seen on Figure 3.3, many images suffer from a vertical stripes pattern with an 8 pixel spacing and variable location on the CCD, especially at low light levels. This variation on the location makes its removal not so trivial. A relation between the pattern and the interference from the triggering of serial CCD read out has been suggested but no confirmed explanation has been found [32]. The same type of equipment with newer firmware version does not seem to suffer from this effect.

A seven pixel horizontal line median filter was first implemented as a solution for the pattern at the cost of some image definition. To reduce this definition loss the filtered and unfiltered image were then weighted through equation (3.7), where $D_f$ and $D$ are the filtered and unfiltered images, and $c$ the weighting factor from equation (3.8).

$$I = c.D_f + (1 - c).D \tag{3.7}$$

$$c = e^{-\left(\frac{D_f}{64}\right)^2} \tag{3.8}$$

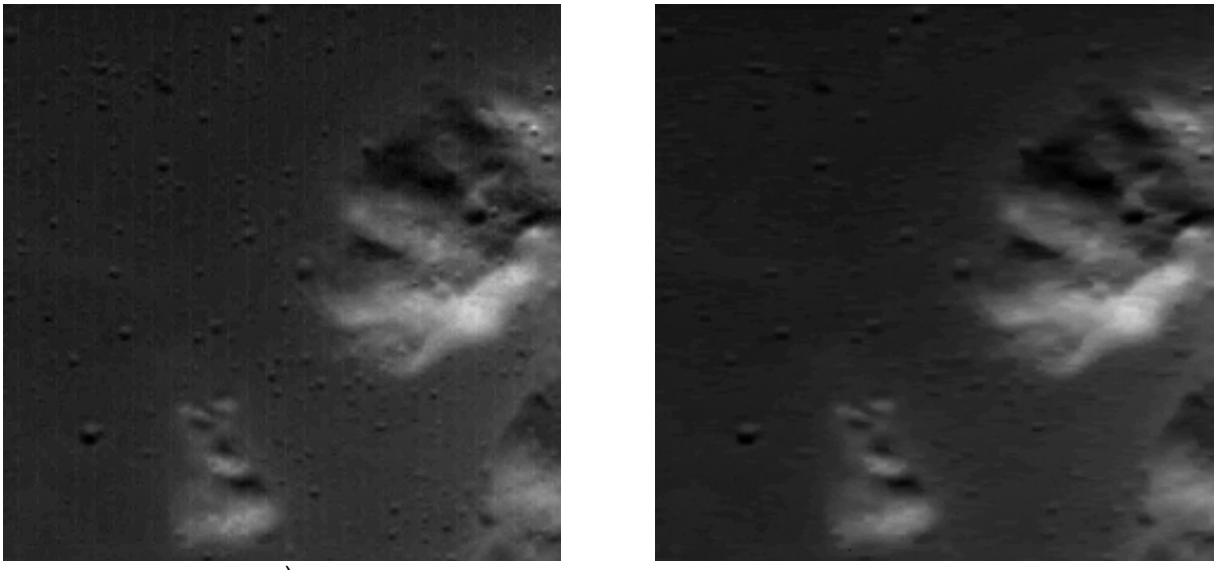

a) b)

Figure 3.3 - a) Zoomed area from image 9 of orbit 2141 before vertical stripes filtering and b) after filtering

Compared with the simple filtering, this method allows the removal of the vertical stripes while preserving the brighter parts without degradation.

### 3.1.3 FLAT FIELDING

After dark current correction the $D_{Corr}$ frame is simply defined by equation (3.9). Having a laboratory blank image with a known radiance $I_0$, constant throughout the pixels, and the exposure time allows recovery of the incoming radiance of the corrected frame. This is achieved by dividing by the laboratory blank image, as presented in equation (3.10). This laboratory blank image is usually referred to as flat field.

$$D_{Corr} = C \cdot I \cdot t_e \tag{3.9}$$

$$I = \frac{D_{Corr}}{D_{flat}} . \frac{t_{e0}}{t_e} . I_0 \tag{3.10}$$

The mentioned increase in dark current accumulation from Earth's radiation belt rendered the flat fields previously acquired in laboratory also unable to provide with an adequate correction. Therefore an in-flight flat field was required.

To achieve it an average of as much frames as possible was made, so that the features in all of them are averaged out and the incoming radiance is the similar for all pixels. The process discarded images with more than one third of dark or saturated pixels, scaled each image to the same brightness by dividing by its median and then computed the mean of all remaining images omitting the saturated or dark pixels. The flat field calculated using in flight data is available on the AMIE dataset on file AMI_LMA_080319_00001_XXXXX.IMG.

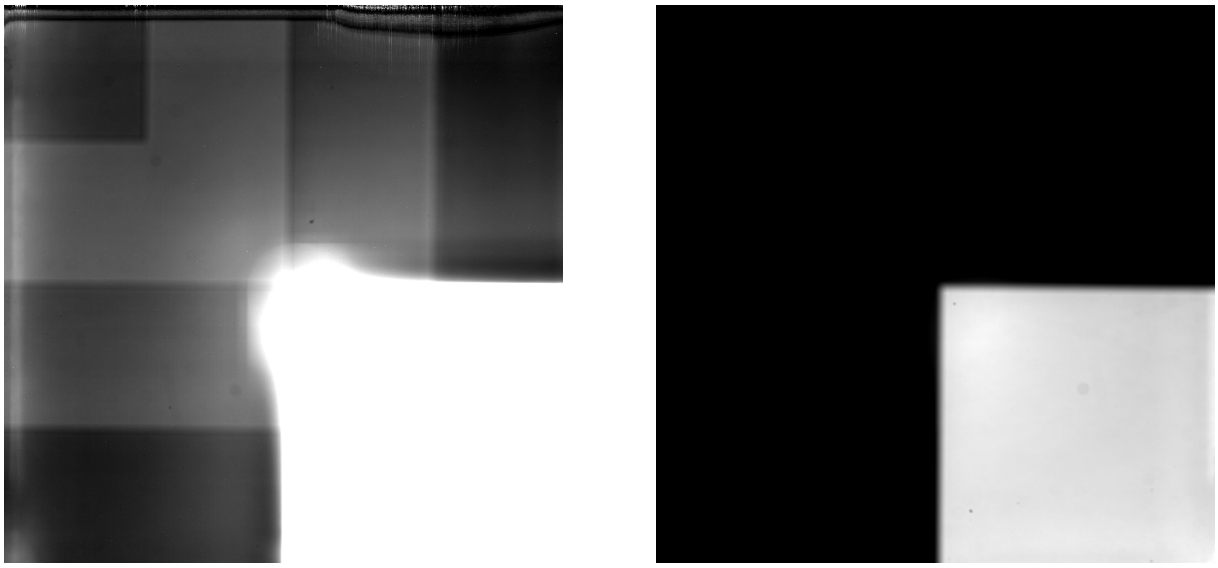

a) b)

Figure 3.4 - a) Flat field computed from in-flight data with grayscale adapted to filter areas. b) Adapted to unfiltered area.

As it can be seen on Figure 3.4 a) the computed flat field from in-flight data has areas with very different brightness levels. That is so it can compensate for intensity attenuation of each of the filters and achieve an usable, visually balanced CCD full frame. It is also noticeable the extreme attenuation the filters caused in comparison with the unfiltered area of the full frame. The brightness difference is so large that no greyscale has enough dynamic to show both areas of the flat field simultaneously, and have to be separately scaled for preview.

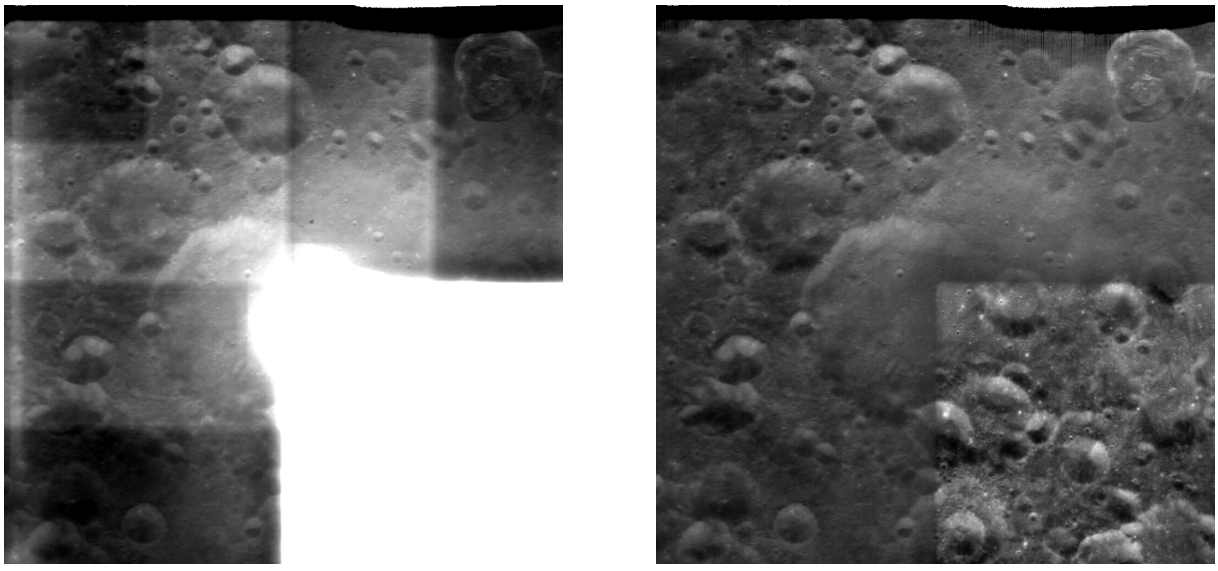

a) b)

Figure 3.5 – a) Full frame 10 from orbit 559 after dark current correction and before flat field correction. b) Full frame after flat field correction

To apply the in-flight flat field the process is the same as for laboratory flat fields, the frame to be corrected is simply divided by the flat field times the exposure time of the captured full frame. Figure 3.5 demonstrates the difference before and after flat field correction.

In the same figure it is also noticeable the contrast difference between filtered and unfiltered areas due to the scattered light. Its large variability across the dataset full frames makes it impossible for the flat field to compensate for this effect.

### 3.1.4 MODEL BRIGHTNESS SCALING

To compensate the different illumination conditions of the images throughout the maps, each frame is scaled using the Hapke reflectance model [33]. The formula for the reflected radiance is given by equation (3.11), where $\omega$ is the soil albedo, $\mu_0$ the cosine function of the incidence angle, $\mu$ the cosine function of the emission angle, $g$ the phase angle and $d$ the distance to the sun. The function B is expressed by equation (3.12) and represents the opposition peak, with $B_0$ and $h$ being two parameters for the height and angular width.

$$I = \frac{|\mu_0|}{(|\mu_0| + \mu)} . \left(\frac{1AU}{d}\right)^2 . [p(g).(1 + B(g)) + H(|\mu_0|).H(\mu) - 1] \tag{3.11}$$

$$B(g) = \frac{B_0}{\left[1 + \frac{\tan\left(\frac{g}{2}\right)}{h}\right]} \tag{3.12}$$

The Chandraeskhar H-function in equation (3.13) was used to approximate the multiple scattering radiance and equation (3.14), suggested by Michael Küppers, the single scattering.

$$H(x) = \frac{1 + 2x}{1 + 2x\sqrt{1 - \omega}} \tag{3.13}$$

$$p(g) = \frac{\pi^2}{5} . \left(\frac{\sin g + (\pi - g).\cos g}{\pi} + \frac{(1 - \cos g)^2}{10}\right) \tag{3.14}$$

To equalize the frames each image is divided by its modelled radiance $I$, with the variable factors chosen to be $B_0 = 0$ and $\omega = 0.12$.

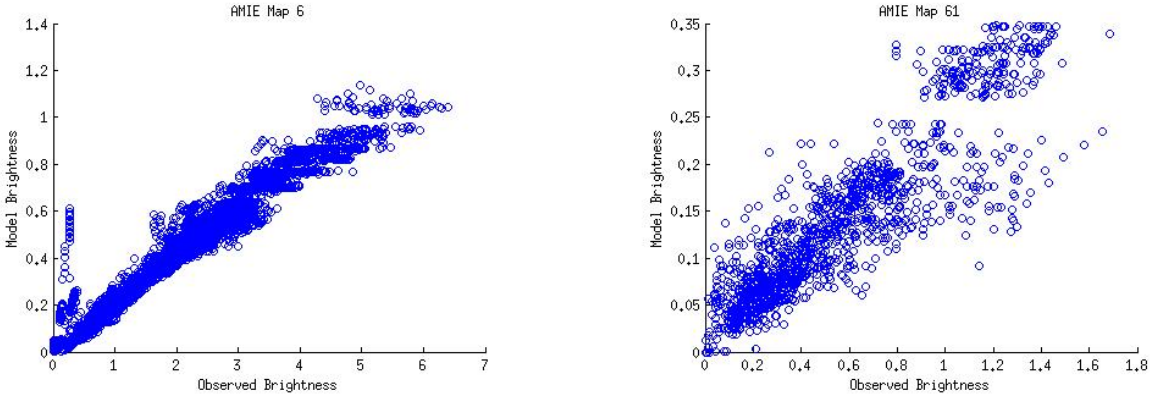


a) b)

Figure 3.6 – a) Correlation between frame observed and Hapke model brightness on AMIE map 6 and b) on AMIE map 61

Despite the high correlation between modelled brightness and effective frame brightness there are cases of frames were the model could not compensate for the illumination conditions, yielding overly dark or bright full frames on the mosaiced map. This is more common in frames with high incidence

angles as noticeable on Figure 3.6 where the observed and the modelled brightness of the frames are compared.
On map 6 (Figure 3.6 a)) which has a medium incidence angle (around 45 degrees) the correlation value between the two is 0.9859 and obtains a good brightness balance on the mosaicked map. On the other hand map 61 (Figure 3.6 b)) has a higher incidence angle (around 75 degrees) and its correlation value is inferior to the previous one having a value of 0.9452. Also its mosaicked map does not have a visually balanced brightness. Trying to further tune the Hapke model parameters did not seem to improve the correlation results.

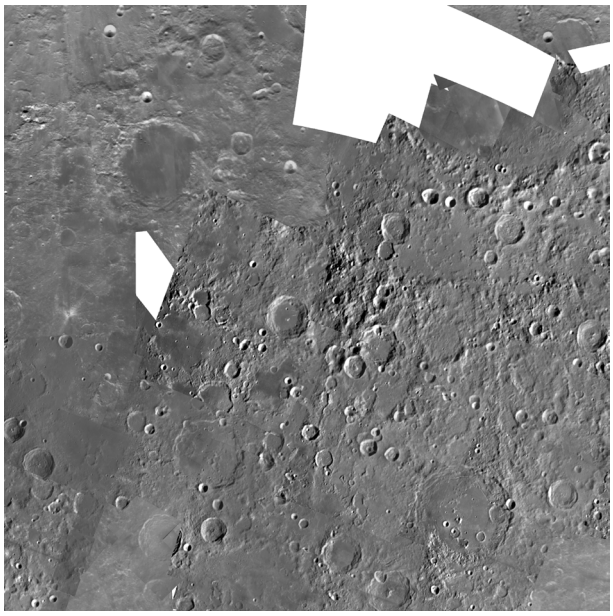

Figure 3.7 - Mosaic of AMIE map 10 using Hapke model brightness scaling

Some full frame images also show an abnormal data median value compared to the rest of the AMIE dataset. Despite having good quality images, these full frames cannot obviously be balanced with the rest of the mosaiced maps by the brightness model scaling, as seen on map 10 presented on Figure 3.7.
For the cases where the limitations of this chapter's brightness scaling severely affects the mosaiced map an empirical scaling method has been implemented and is described in chapter 3.4.3.

### 3.1.5 Corrupted 128 Pixel Blocks

It was detected that a reasonably large number of frames had one or more square blocks of 128 pixels with values that largely differed from the rest of the frame. As shown in Figure 3.8 this corrupted blocks appeared randomly on an 8 by 8 position grid of the full frame. It is apparently unrelated with the quality or light conditions, extending through a large type of different frames.

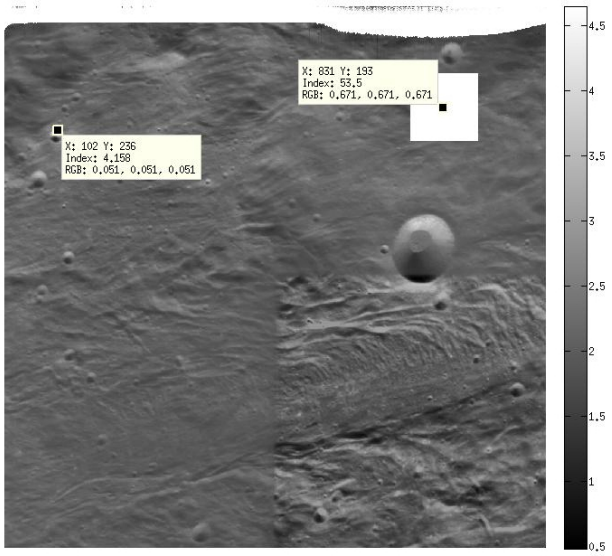


Figure 3.8 - Image 18 from orbit 40 with a corrupted block

Since most of these blocks had no visible features and extremely larger data numbers compared to the rest of the frame it severely affected any operation on the frame that included them (e.g. mean, median, maximum value…), albeit their constant positioning allows for a possible detection and removal from mosaicing.

To use the frame without being affected each block is tested for corruption using the steps:

- The frame is divided into an 8 by 8 grid, leaving 64 individual blocks of 128 pixels.
- The mean, minimum and maximum is computed for each block.
- The mean of the full frame is computed, excluding areas of the where the corresponding block has a mean value inferior to 0.
- Each block is then marked as corrupted if its mean value is the same as the maximum or the minimum, its maximum value is less than or equal to 0 and if its mean value is largely greater than the mean value of the entire full frame.

For the comparison between the block and the full frame mean it was chosen to mark as corrupted blocks where its mean was 15 times bigger than the frame value. This value allows to correctly detect most of the blocks without false positives from frames with low angle illumination, which are mostly composed of large dark areas and small visible mountainous tops. The result of the test is then subsequently used to exclude the marked areas from any required computation.

Despite the exclusion of the detected corrupted areas there are still a smaller number of corrupted blocks that have no discernible variation of data numbers in relation to the rest of the frame. For those a detection method could not be obtained.

Using the dataset classification process described on chapter 3.3.1.1 the full frames with detectable corrupted blocks were marked as damaged. After the process was complete 530 full frames were detected and marked as damaged.

### 3.1.6 SCATTERED LIGHT

The flat fielding process equalized the mean brightness between filtered and unfiltered areas of the AMIE full frame, but there was still a discernible contrast difference between them. This effect is due to scattered light beneath the filters and is especially strong on the border between the two areas, near the centre of the frame, reducing exponentially as it radially distances from it. It leaded to the conclusion that the scattered light must get beneath from the side of the filters and is absorbed as it bounces between them and the CCD [32].

If the scattered light had a constant effect on all frames it would have been removed by the flat fielding process, but that is not the case. The noticeable brighter filters from Figure 3.9 are an indication of above average scatter and, as there is above cases, there are also frames with below average and darker filters area making its removal difficult.

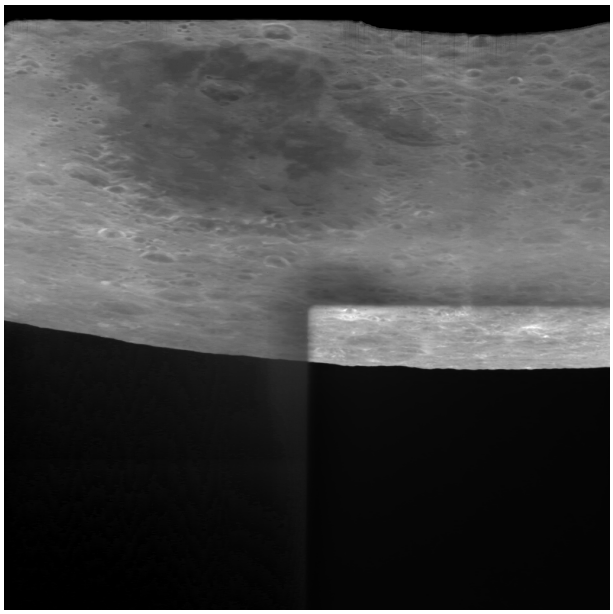

Figure 3.9 - Full frame from image 1 of orbit 2865 with noticeable scattered light

A process for the scattered light removal has previously been proposed by Björn Grieger [34]. This method had the tendency to overestimate the amount of scattered light, yielding too dark filters areas. Therefore, a different approach has been taken to this problem.

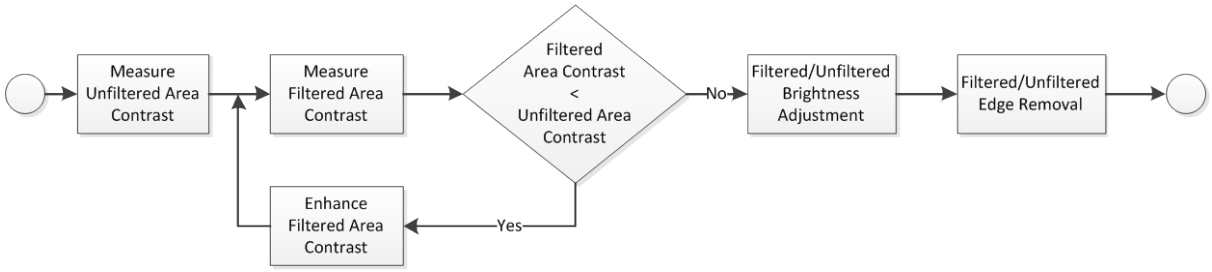


Figure 3.10 - Scattered light compensation process

Since the main problem caused by the scattered light is the reduced contrast on the filtered areas, in comparison to the unfiltered areas, a more direct approach can be taken by increasing the contrast where needed. As Figure 3.10 describes, to do so first the contrast of both areas is measured and compared. If needed, the filters area of the frame is then increased in contrast until both areas have similar values. When this is achieved the possible differences in brightness and edge between the filtered and unfiltered areas are adjusted.

The process is described in detail below. Chapter 3.1.6.1 details the Retinal-like Subsampling Contrast (RSC) which is the contrast measurement algorithm used to compare the contrast between the areas of the full frame.
Following the execution order, is then presented in chapter 3.1.6.2 the contrast enhancement technique. This is a combination of two methods, the Modified Partially Overlapped Sub-block (MPOS) and the Discrete Cosine Transform (DCT) contrast enhancement. It is therefore called MPOS-DCT.

Finally, in chapter 3.1.6.3 the brightness adjustments needed to compensate for the contrast enhancement are detailed.

#### 3.1.6.1 RSC CONTRAST MEASURE

In order to compare the contrast of different images a contrast measure which provides a result that highly correlates with the human optical perception of contrast is needed. However, the measurement and evaluation of contrast and contrast changes in arbitrary images are not uniquely defined in the literature [35], and perceptual contrast is strongly defined by the contextual influence on the observer task and experience.
A few different methods were tested for this purpose but the one found to be the better fit was defined as Retinal-like Subsampling Contrast (RSC) [36]. The version used and described below is a slightly modified one with a one value per image measurement result.

To achieve the contrast evaluation the image is transformed into a multilevel pyramidal structure. Each level is obtained by subsampling the image from the previous level to half the size, starting from the original image. In this case each image was subsampled into levels, until one of its dimensions fall beneath 4 pixels.

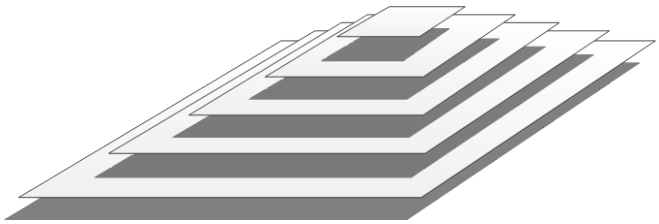

Figure 3.11 - RSC multilevel pyramidal structure example

$$DOG(x,y) = R_c(x,y) - R_s(x,y) \tag{3.15}$$

Then, for each level, the computation of the difference of Gaussians (DOG) is performed. The conventional DOG model, presented in equation (3.15), is defined by the difference between the central $R_c$ and the surround $R_s$components. The components $R_c$ and $R_s$ are the level image after being filtered with two different Gaussian filters, with radius $r_c$ and $r_s$.respectively. This is because it assumes a retinal ganglion cell or an LGN neuron response is only dependant on the luminance difference. After the light adaptation process a neuron is also dependant on the local luminance average. Therefore, the model should be adapted. Tadmor and Tolhurst [37] suggested equation (3.16) as solution.

$$DOG_L^{TT}(x,y) = \frac{R_c(x,y) - R_s(x,y)}{R_c(x,y) + R_s(x,y)} \tag{3.16}$$

The contrast of each level image will then be the average value along the modified $DOG_L^{TT}$ (equation (3.17)) on the positions where the level image has data values above a defined minimum value.

$$C_L = \frac{1}{n_{sum}} \times \sum_{i=1}^{i_{max}} \sum_{j=1}^{j_{max}} DOG_L^{TT}(i,j)\,[Img_L(i,j) > minVal] \tag{3.17}$$

Where $i_{max}$ and $j_{max}$ are the dimensions of the level image and $n_{sum}$ the number of pixels of the level image $Img_L$ that have data values above $minVal$. This minimum value is a data value that allows excluding the portions of the image that are on shadow portions of the terrain, and the way it is determined follows equation (3.39) that is described below on chapter 3.4.3.

$$C^{RSC} = \frac{1}{n} \times \sum_{L=1}^{n} C_L \tag{3.18}$$

The overall contrast of the original image $C^{RSC}$ will be the average of the previously acquired levels contrast values, as expressed by (3.18) with $n$ being the number of levels. As radius for the Gaussian filters were used $r_c = 2$ and $r_s = 4$.

#### 3.1.6.2 MPOS-DCT CONTRAST ENHANCEMENT

Image enhancement techniques can be divided into direct and indirect enhancement methods. Indirect refer to methods that enhances the image contrast without measuring its contrast, while direct methods establish a contrast measure criterion and improve the image contrast directly according it. [38]

It can also be made the distinction between global and local contrast enhancement. Global methods are usually less complex and computational faster, but achieve less satisfying results as they treat the whole image as a block and make no distinction between different areas. Local enhancement methods divide the image into different areas with far more satisfying results, but their complexity can be a problem when real-time computation is needed or speed is a factor.

Since the dataset include a large number of full frames the processing time is an aspect that must be taken into account, otherwise the time needed to mosaic an AMIE map will be too long. The adopted technique is a direct local enhancement technique that is a combination of modified versions of methods proposed by Tang [38] and Kim [39]. It uses the discrete cosine transform (DCT) as a basis for contrast enhancement and a modified partially overlapped sub-block (MPOS) for local enhancement block effect removal. The DCT enhancement method offers the same enhancement quality but with less computation requirements than other equivalent methods.

Below the discrete cosine transform enhancement is described in detail (chapter 3.1.6.2.1) as well as the modified partially overlapped sub-block (chapter 3.1.6.2.2).

##### 3.1.6.2.1 DCT CONTRAST ENHANCEMENT

The method proposed by Tang [38] takes advantage of DCT-based image compression standards such as JPEG, MPEG2 and H.261, in which the images are divided into 8x8 non-overlapping pixel blocks and computed the two dimensional DCT of each block. By modifying the DCT coefficients the image contrast can be improved without affecting the compression and even reducing storage requirements. Despite being thought to use the compression standards the method is not limited in its use, and can be widely applied to any image. In this case, the contrast enhancement is applied without the limitation of 8 by 8 pixel blocks made by the compression standards.

The process begins by first performing the two-dimensional DCT, as it happens with the original method, which returns a matrix of coefficients. Each coefficient represents the contribution of a waveform with these being ordered in increasing spatial frequencies from the top left of the resulting matrix, as exemplified in Figure 3.12.

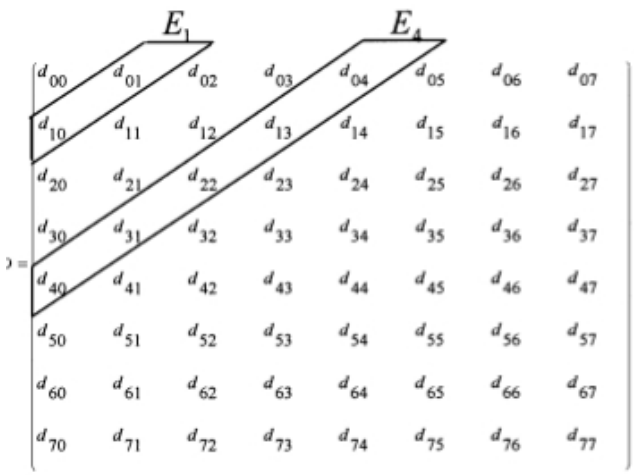


Figure 3.12 - Example of an 8x8 pixel DCT matrix coefficients with the 1st and 4th bands highlighted [38]

This provides a natural way of measuring contrast by using Peli's [35] contrast definition, that states that human contrast perception is based on the difference between the high and low frequency content. By grouping the coefficients into frequency bands the contrast can then be defined using equation (3.19), where $E_n$ is the average amplitude over the band n, and defined by equation (3.20).

$$C_n = \frac{E_n}{\sum_{t=0}^{n-1} E_t} \tag{3.19}$$

$$E_t = \frac{\sum_{k+l=t} |d_{k+l}|}{N} \tag{3.20}$$

Since the objective is to increase the contrast uniformly over all frequencies, the new contrast coefficients $\overline{C_n}$ will be related to the previously acquired coefficients $C_n$ by the constant contrast increase value $\lambda$. Solving equation (3.21) allows finding that the new DCT $\overline{d_{k,l}}$ matrix coefficients are given by equation (3.22).

$$\overline{C_n} = \lambda . C_n \tag{3.21}$$

$$\overline{d_{k,l}} = \lambda . H_{k+l} . d_{k,l}, \qquad n \geq 1 \tag{3.22}$$

Where,

$$H_{k+l} = \frac{\sum_{t=0}^{n-1} \overline{E_t}}{\sum_{t=0}^{n-1} E_t}, \qquad k + l \geq 1 \tag{3.23}$$

After the $\overline{d_{k,l}}$ matrix coefficients are computed the inverse discrete cosine transform is performed and the contrast improved image recovered.
The DCT contrast method allows for both contrast intensification and reduction. For $\lambda$ values above 1 the contrast is intensified. For values between 0 and 1 the image contrast is reduced.

#### 3.1.6.2.2 MPOS Local Contrast Algorithm

The previously described contrast enhancement method is based on 8x8 pixels blocks, but this carries high computation requirement that are not necessary for uncompressed images. Due to the high number of images in the dataset this would also increase the AMIE maps building time beyond acceptable levels. Therefore, a 128 by 128 pixel block size method was established without much contrast adjustment deficit.

Local contrast enhancement techniques have the tendency to suffer from blocking effects, where borders between adjacent blocks have different brightness levels. As it can been seen on Figure 3.14, this has a tendency to become more noticeable as the block pixel size increases. To compensate for this effect a modified method based on Kim's [39] previously proposed one was implemented. It uses an image weighting system between images with three different blocks dispositions, instead of the simple overlapping blocks proposed. This allows for bigger block sizes without the blocking affect becoming significantly noticeable, which reduces the needed computation.

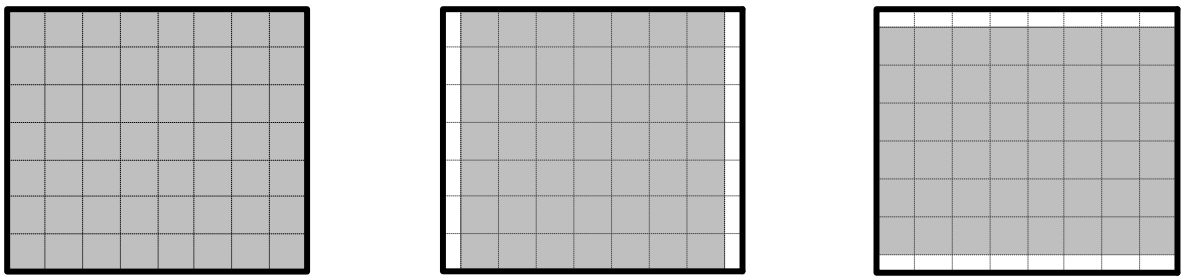

a) b) c)

Figure 3.13 - a) Block disposition over the full frame of the enhanced imaged. b) Block disposition on the vertical compensation image. c) Block disposition on the horizontal compensation image.

To begin the process the image is divided into 128x128 non-overlapping pixel blocks and on each block the DCT contrast enhancement is applied. Taking into account that the top 128 pixels of the images have been removed due to dark current accumulation this creates 7 by 8 matrix of blocks over the image.
To compensate for the vertical borders of the blocking effect another pass is made over the image now with half of the block size (in this case 64 pixels) of horizontal phase difference from the first. To compensate for the horizontal borders the same process is made but with half of the block size of vertical phase difference instead.

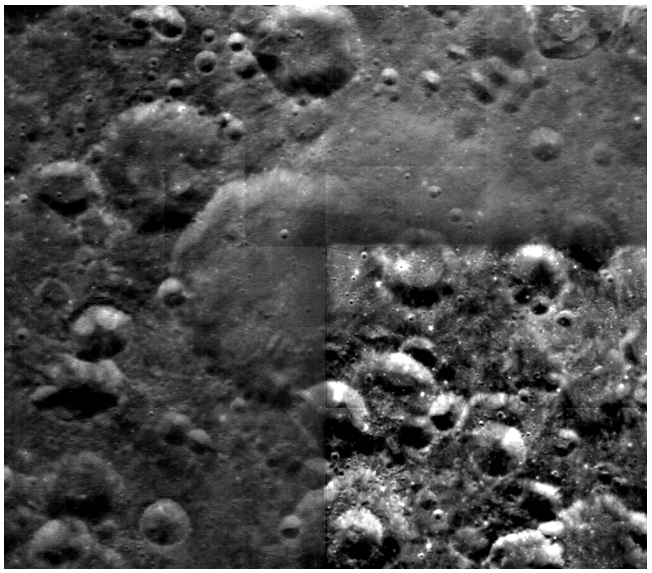

Figure 3.14 – Full frame 10 from orbit 559 without compensation and noticeable blocking effect

Each blocking effect compensation image is then weighted over a matrix, with values varying from 0 to 1. The maximum values are located over the blocking effect borders to be removed and reduces as it furthers away from it, reaching zero at the centre of the blocks. For simplicity the contrast improvement for compensation is applied over the full frame even though the changes to the unfiltered area of the frame are of no interest.

The effect of the brightness difference between filtered and unfiltered areas needs to be removed from the process to avoid undesirable propagation. To ensure this, the problematic areas of the compensation are weighted out. These areas are the large strips with 0 value on the weighting matrixes of Figure 3.15.

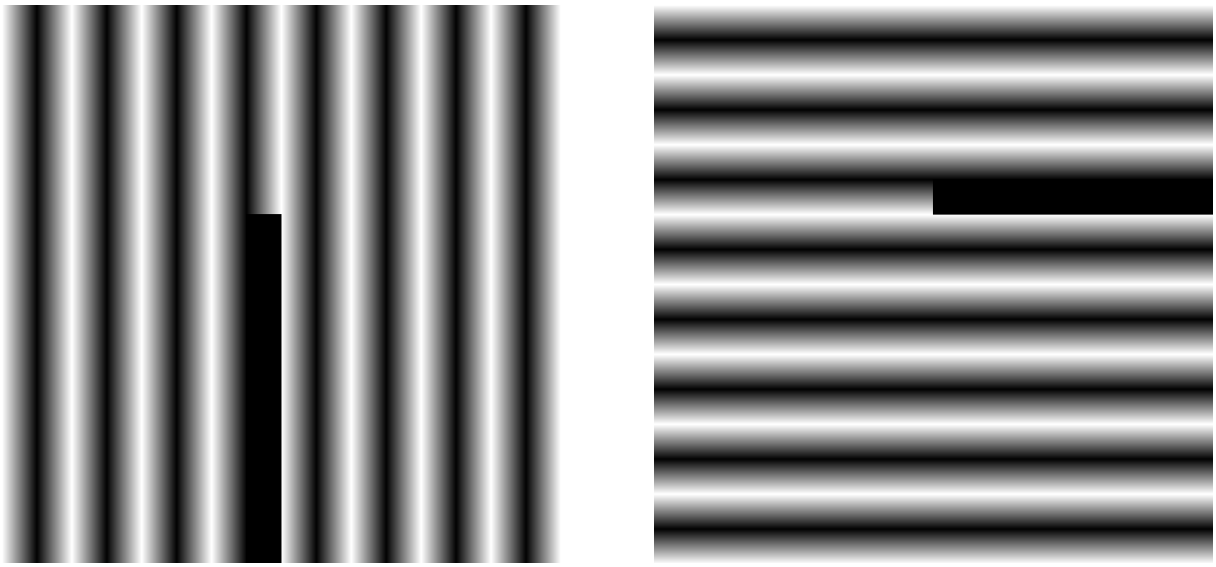

a) b)

Figure 3.15 - a) Compensation weighting matrix for the vertical borders of blocking effect. b) Weighting matrix for the horizontal borders

$$I = I_0.W_{img} + W_{Comp}.(I_V.W'_V + I_H.W'_H) \tag{3.24}$$

The three images are weighted using equation (3.24), where $I_0$ is the uncompensated contrast enhanced image, $I_V$ and $I_H$ the blocking effect compensation images for vertical and horizontal borders and $W_{img}$ and $W_{Comp}$ the weighting matrixes for contrast improved image and the overall blocking effect compensation.

$W'_V$ and $W'_H$ are the balanced weighting matrixes, as they need to be balanced against each other to mathematically ensure that the compensation is not weighted above 1. This is simply achieved by equations (3.25) and (3.26), with $W_V$ and $W_H$ being the unbalanced matrixes of Figure 3.15.

$$W'_V(x,y) = \frac{W_V(x,y)}{W_V(x,y) + W_H(x,y)} \tag{3.25}$$

$$W'_H(x,y) = \frac{W_H(x,y)}{W_V(x,y) + W_H(x,y)} \tag{3.26}$$

The compensation weighting matrix is then the maximum value between the vertical and horizontal weighting matrixes on each position (equation (3.27)). The contrast enhanced image weighting matrix is then the inverse value on each of the positions of the compensation matrix (equation (3.28)).

$$W_{Comp}(x,y) = \max\big(W_V(x,y);\, W_H(x,y)\big) \tag{3.27}$$

$$W_{img}(x,y) = 1 - W_{Comp}(x,y) \tag{3.28}$$

Since on each of the 64 pixels closest the both sides there is only the need for horizontal compensation, as well as on the 64 closest to the top and bottom there is only for vertical, a final adjustment has to be made. Therefore the image weighting matrix is recovered using equation (3.28) and performed the adjustment on the sides, top and bottom. Then, the updated compensation

weighting matrix is reconstructed through the inverse process. In Figure 3.16 the final weighting matrix $W_{img}$ can be seen.

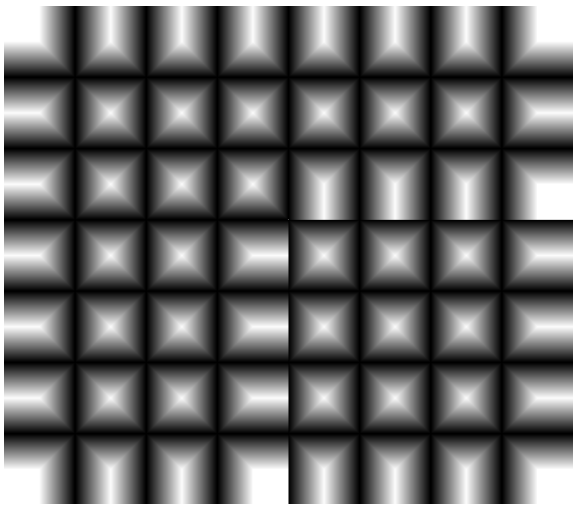

Figure 3.16 – MPOS primary image weighting matrix

After all the weighting matrixes are produced, the final contrast improved image can be recovered using equation (3.24). The contrast balanced full frame is then the combination of the enhanced filtered area of the full frame and original unfiltered area. As noticeable in Figure 3.17, albeit in some images there is still a small effect from scattered light near the border between filtered and unfiltered areas, its effect has been greatly reduced and full frame appears visually more balanced.

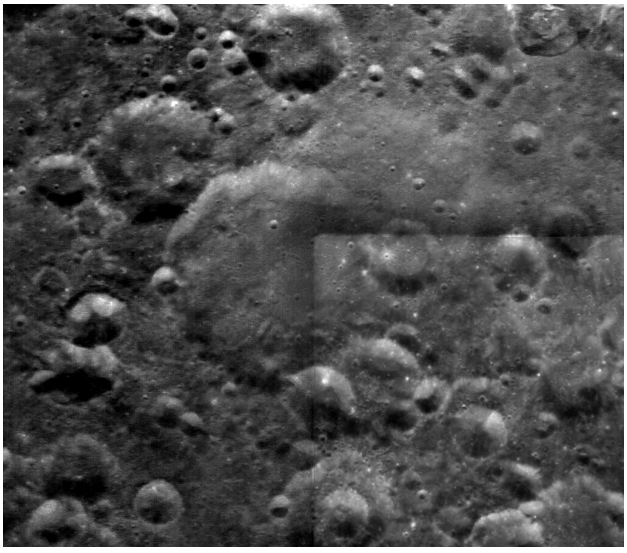

Figure 3.17 - Full frame 10 from orbit 559 after contrast balance

#### 3.1.6.3 BRIGHTNESS ADJUSTMENTS

After the full frame has been contrast measured by the RSC contrast measure and the contrast difference of filtered and unfiltered reduced by MPOS-DCT contrast enhancement a mean brightness difference is present between both areas. This is created by the scattered light effect previously existent on the frame as well as the process of contrast enhancement.
To normalize the different areas brightness, the mean value of the pixels closest to the border between both is computed, and the filtered area brought to the same value as the unfiltered.

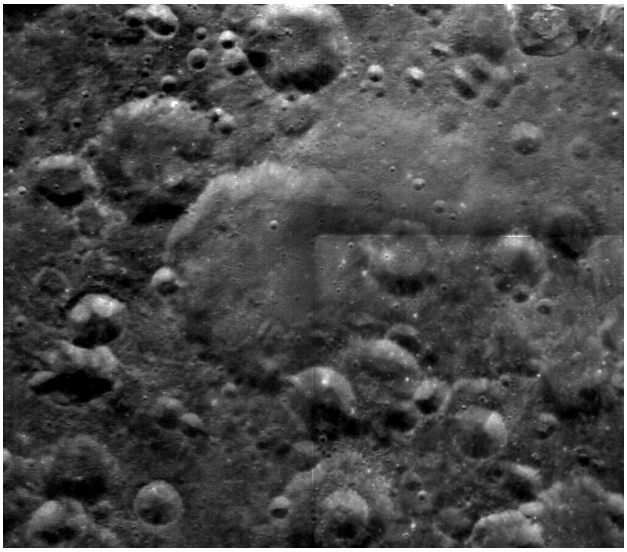

Figure 3.18 - Full frame 10 from orbit 559 after brightness balance

Before it is complete there is yet a visually unpleasant line edge between filtered and unfiltered derived from the previously described brightness adjustment. A smoothing filtered passed only over the edge is applied to make it less noticeable.

| | | | | | | | |
|---|---|---|---|---|---|---|---|
| | | | | | | | |
| 150 | 155 | 158 | 2 | 5 | 165 | 172 | 165 |
| 165 | 170 | **168** | **166** | **164** | **162** | 160 | 162 |
| 145 | 131 | **135** | **139** | **143** | **147** | 151 | 154 |
| 140 | 142 | 153 | 10 | 7 | 133 | 176 | 168 |
| | | | | | | | |
| | | | | | | | |

Figure 3.19 - Edge smoothing filter example

Figure 3.20 a) shows the prominent low brightness edge only covers the two pixels closest to the frontier between areas on each side. The mean value between the third pixel on each side (underlined on Figure 3.19) of the frontier is computed and divided by the five steps needed to go from one pixel to the other. Using this value as step size, the pixels in between are added (or subtracted, depending on the case) the step size value times the steps already taken from the starting position, thus smoothing the edge. The pixels modified during the process are represented in bold in Figure 3.19.

This simple filter effectively removes the edge without compromising the full frame's image definition.

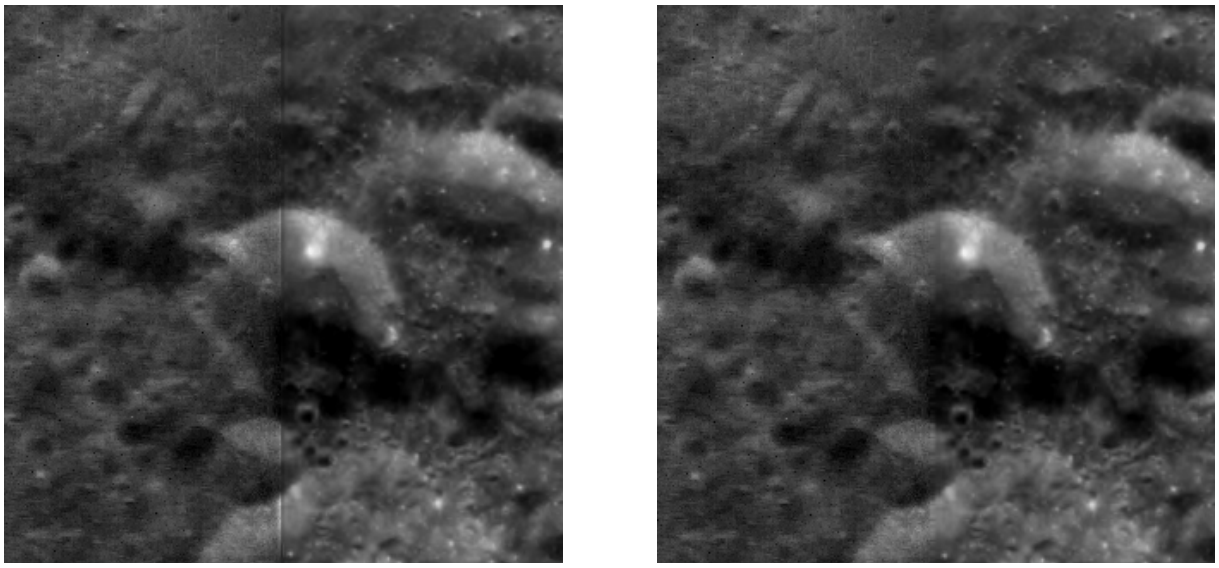

a) b)

Figure 3.20 - a) Zoomed area of the full frame 10 from orbit 559 before smoothing filter. b) After smoothing filter.

## 3.2 AMIE MOON ATLAS ORGANIZATION

The AMIE frames have a higher resolution on the southern hemisphere, particularly on the area near the South Pole where resolution of 27m/pixel is available. The AMIE coverage resolution is described in detail in Figure 3.21. The maps are built with 3000 by 3000 pixels resolution, as this allows for adequate printing at 25 cm by 25 cm pages with 300 ppi (considered standard for professional printing quality [40]).

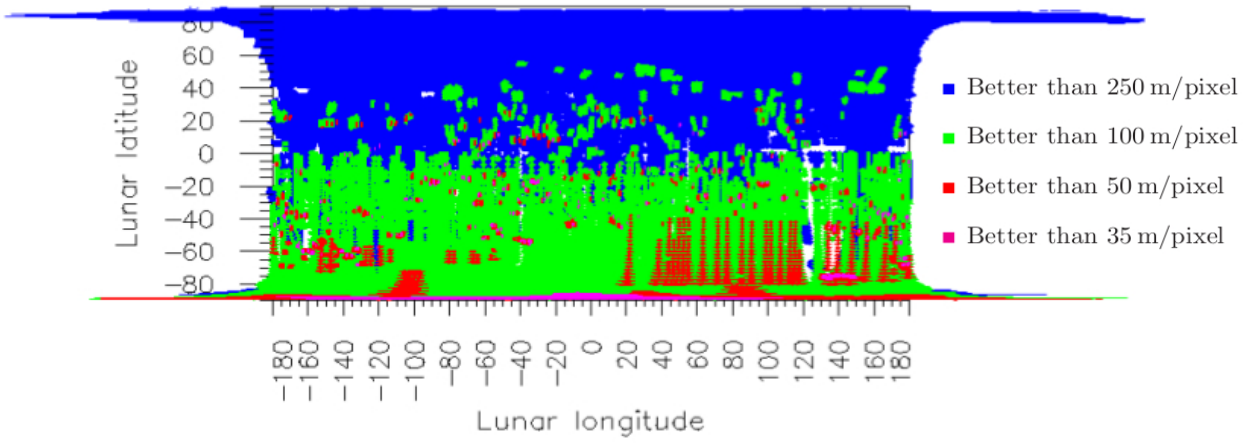


Figure 3.21 - Coverage and resolution of AMIE full frame images [34]

To take advantage of the available resolution, the Moon was divided into square maps with minimal distortion and variable coverage. The maps in the northern hemisphere, closer to the north pole, cover a larger area to guarantee a reasonable image resolution. As the maps approximate south the coverage is reduced, as described in Figure 3.22 and Table 3.1. For latitudes between 75° S and 60° N it is used a Mercator projection. For latitudes higher than this the stereographic projection is used.

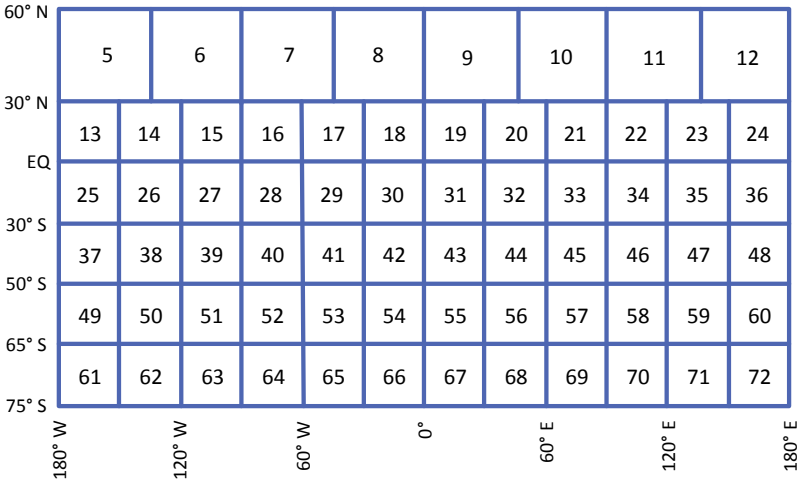


Figure 3.22 - AMIE more equatorial maps coverage area

Table 3.1 - AMIE maps detailed information

| Latitude | Projection | Number of maps | Width [degrees] | Width [Km] | Resolution [m/pixel] |
|---|---|---|---|---|---|
| **60°N-90°N** | Polar | 4 | 30° | 900 | 300 |
| **30°S-60°N** | Mercator | 32 | 30° | 900 | 300 |
| **50°S-30°S** | Mercator | 12 | 20° | 600 | 200 |
| **65°S-50°S** | Mercator | 12 | 15° | 450 | 150 |
| **75°S-65°S** | Mercator | 12 | 10° | 300 | 100 |
| **90°S-75°S** | Polar | 16 | 7,5° | 250 | 85 |

The north pole of the Moon was divided into four maps (numbered 1 through 4), covering a radius of over 30° of latitude with a resolution of 300m/pixel (Figure 3.23 a)).
The South Pole, where the average full frame resolution is much higher, was divided into 16 maps. These extend through a radius of over 15° of latitude and have a resolution of 75m/pixel (Figure 3.23 b)).

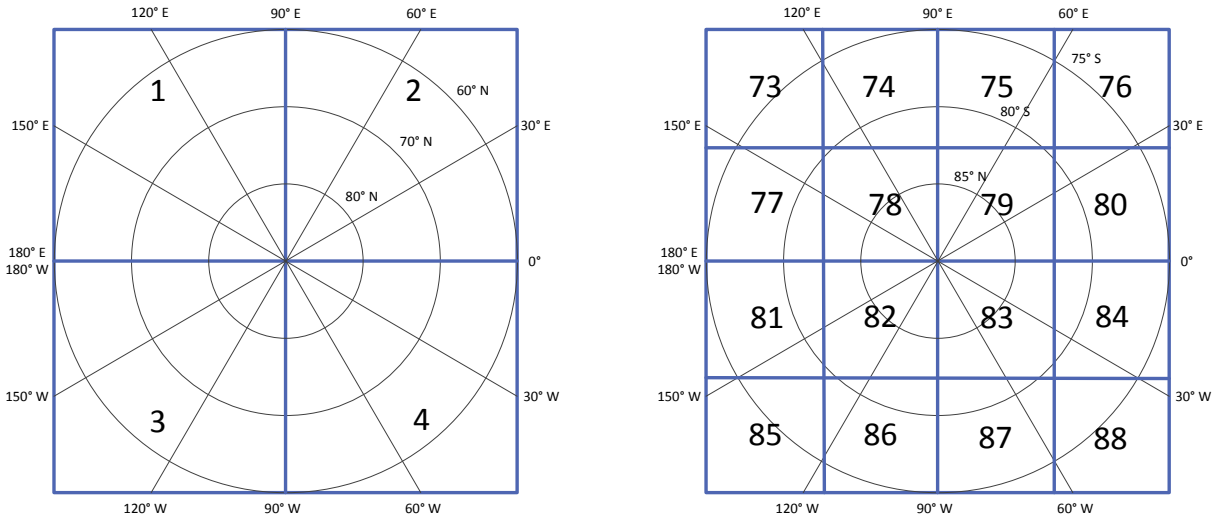


a) b)

Figure 3.23 - a) AMIE North pole map area coverage and b) South pole map area coverage

### 3.2.1 Geometric Computation and Pointing Accuracy

The geometric computation of the full frames, acquired by the AMIE instrument, was done using SPICE (Spacecraft, Planet, Instrument, Camera-matrix, Event) [41]. This system developed by NASA keeps all the required information in the so-called SPICE kernels that can be loaded into it.

The SPICE kernels include the corners of the field of view of the instrument, the orientation of the instrument in relation to the instrument frame, the altitude of the spacecraft in relation to the on-board clock count, the relation between the on-board clock count and ephemeris time and position of the spacecraft in dependence of ephemeris time. Also included is the radius of the Moon, its orientation taking into account Moon's libration with high precision, leap seconds record that related ephemeris time with universal time and the position of the solar system bodies with respect to the solar system barycentre in dependence of time.

In addition to this information, for further processing, there is the need for the full frames acquisition time. Since this was not tagged in the spacecraft telemetry, the acquisition time was instead computed using the acknowledgment of the "take image" command and the knowledge of the delay between the command and acquisition time. With this information, it is then possible to intersect with the viewing

direction of the instrument and achieve the image positioning on the lunar surface. The error on this positioning is always dominated by the uncertainty of spacecraft pointing.

In Grieger et al. [42] the pointing accuracy of AMIE captured images was studied. It was detected an offset from the Clementine base map mosaic which was not constant through the moon. Previous studies of this base map showed inaccuracies between Moon's original locations according to the archived SPICE kernels and the mosaiced USGS' map. While at Apollo locations low deviation was found this value increased by 10 times on other areas.
The comparison between the Clementine base map deviation and the AMIE detected offset showed a very good correlation, leading to the conclusion that the offset was an effect of base map inaccuracies itself.

## 3.3 MAP MOSAICING

After the calibration is performed, and knowing the distribution of the AMIE Moon maps on the lunar surface, the map mosaicing can begin.

In order to create a visually balanced mosaiced map it is important to choose the more adequate available images, and those who can create a map with homogeneous illumination. For that purpose a good selection of the full frames out of the dataset is needed, especially the order to which they are presented for mosaicing. The selection, classification and ordering the full frames to be mosaiced is described on chapter 3.3.1.

The process of projection over the map is described in chapter 3.3.2.

### 3.3.1 DATA SELECTION, ORDER AND ILLUMINATION CLUSTERING

First it is important to classify the dataset full frames according to their visual quality and usable areas of the frame, which is explained in chapter 3.3.1.1. Then the order in that they are projected also takes a relevant role. The images with more quality that share similar illumination conditions with the larger number of others should be projected first to ensure the best possible map.

To order it, the map list of full frames is first divided into two groups, separating the full frames with good quality (classification 1 up to 3) from those with doubtful quality (classification 4 up to 6). For that purpose, each full frame was individually analysed by an operator using the classification described in chapter 3.3.1.1.

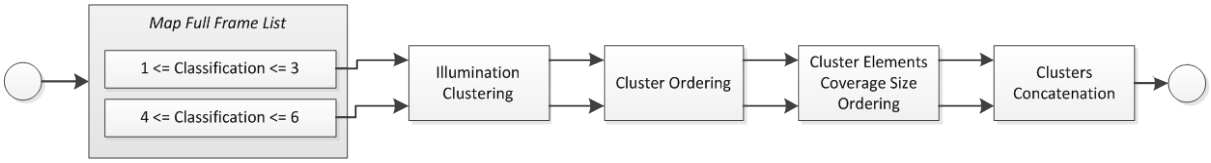


Figure 3.24 - AMIE map data selection and ordering process

Following the process described in Figure 3.24, the full frames on each of the groups are then clustered according to their illumination conditions. During that process the images are clustered, the created clusters are ordered according to illumination of the cluster and images on each of the clusters ordered following the area coverage of the full frame. The clustering procedure, as well as the ordering of the clusters, is described in detail in chapter 3.3.1.3. Before that, an overview of the AMIE dataset illumination conditions is presented in chapter 3.3.1.2.

When the clustering is complete for both groups of images they are re-assembled, with the group of images marked as good quality being on top of the new ordered list sent for projection.

#### 3.3.1.1 FULL FRAME CLASSIFICATION

The variation on the Moon's soil reflectance combined with the variable exposure time and filters response created frames with under or overexposed areas. The calibration process reduced this effect, compensating the radiance and contrast differences, but some parts or complete frames were still not adequate for mosaicing on a map.

To remove the damaged areas while maximizing the available data, each frame was manually classified initially into one of four classes. Later, for an even more complete distinction on the frame quality, three more were added for a total of seven.

Table 3.2 - Classification of the Smart-1 AMIE full frame dataset

| Class | Characteristic | Number of Frames |
|---|---|---|
| **0** | Unusable frame | 7707 |
| **1** | Usable only on the non filtered area | 514 |
| **2** | Usable only on the filtered area | 4012 |
| **3** | Full frame usable | 16007 |
| **4** | Usable only on the non filtered area but with doubtful quality | 45 |
| **5** | Usable only on the filtered area but with doubtful quality | 568 |
| **6** | Full frame usable but with doubtful quality | 3092 |
| **Total** | | 31945 |

As presented on Table 3.2, each full frame was divided into two distinct areas (filtered area and unfiltered area) and classified according to their quality. Classes 4 to 6 were added to account for frames with lower quality or low light conditions that did not fit into classes 1 to 3 qualities but could still be used in case the latter weren't enough to fill the mosaic.

Figure 3.25 - Full frame 2 from orbit 771 with overexposed unfiltered area.

Frames with no data, dark sky, frames from earth and frames were it can be seen the sky or the moon were classified as class 0. To this class were also added frames with virtually no visible Moon's soil due to low light.
A large number of frames were detected with damaged unfiltered area as in Figure 3.25. These were not only overexposed as well as the flat fielding appeared overcorrect this area, yielding it too dark and with low dynamic range compared to the filtered area.

#### 3.3.1.1.1 CLASSIFICATION TOOL

The classification process consisted in individually viewing each image of the AMIE dataset, manually attributing a classification, store the classification associated with that full frame on the information

database and mark it as manually classified. Since the dataset is quite extensive a tool that would ease this manual process and make it more efficient was needed.

This tool (Figure 3.26) was designed with speed and ergonomy in mind for the lengthy classification. While the current full frame image to be classified is presented on the left of the tool, the controls and currently visualised image details are located on the right side. To minimize errors, buttons larger than normal were used and graphical aids added. The operator can also control the tool directly from the keyboard, with the keyboards' numbers associated with the evaluated classification and arrows for image skipping control.

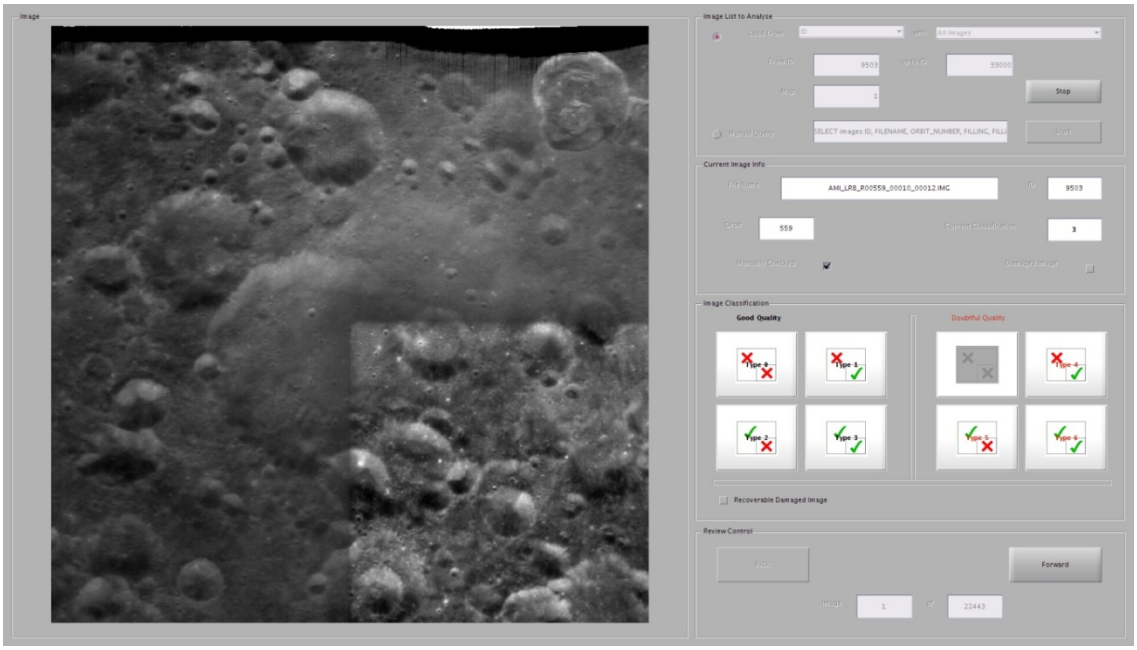


Figure 3.26 - AMIE dataset classification tool

To ensure that the correct full frame image was presented to the operator, each image greyscale was scaled to the full frame, excluding the previously mentioned top band near the readout. Also the detected 128 corrupted pixel blocks (see chapter 3.1.5) were excluded so that the dynamic visualisation range wouldn't be overestimated and the image overly dark. Upon detection of a corrupted block, a flag warning the operator is activated and the detection flag stored to database along with the classification.

#### 3.3.1.2 ILLUMINATION CONDITIONS OVERVIEW

Figure 3.27 shows the relation between the illumination angles, with the sun being represented by vector *J* and the observer by vector *I*. The illumination incidence angle *i* is the angle made the sun and the normal vector to the plane, while the emission angle *e* is the one between the observer and the plane's normal. The illumination is then phase angle *g* is the angle made by the sun and the observer.

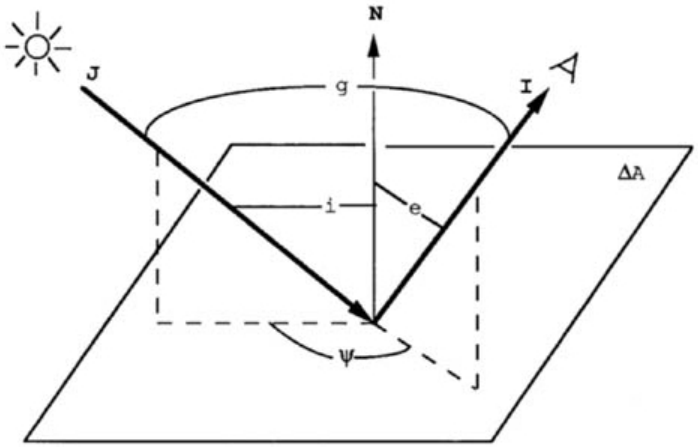


Figure 3.27 - Illumination angles

On the dataset, full frames with low illumination phase angle (equal to or below 30 degrees) show a very small amount of discerning features and small contrast definition, regardless of the type of terrain they cover. A similar effect even though with good contrast definition happens to full frames with very high phase angles (equal to or above 80 degrees). These are covered with excessive shadow areas and therefore also present a small amount of visible features. The latter case is found primarily on images captured on the poles area.

As with low phase angle, even though not so severely, low incidence angle also have a small amount of features and contrast definition. High incidence angle have excellent contrast definition but some noticeable shadows from craters or high terrain, while medium values have an intermediate contrast but do not suffer from the effect of shadows.

As was seen in Figure 3.27, the illumination emission angle is closely related with incidence and phase, especially if the angle $\psi$ is close to 90°. Therefore, when there is an increase on the emission angle there is also an increase on the difference between incidence and phase angles. Full frames with smaller emission angles, and incidence and phase angles closely related, have better feature definition. That effect is more noticeable on images with higher phase angles, as they generally have higher image contrast.

#### 3.3.1.3 ILLUMINATION CLUSTERING

The illumination clustering aims at adequately grouping the list of full frames according to their characteristics for further processing and ordering. As the illumination conditions provide a fairly appropriate overall indicator of those characteristics the illumination incidence, emission and phase angles are used as parameters for clustering.

For this type of data, the Ward's linkage that uses the squared Euclidean distance is a good choice as clustering method. This linkage uses equation (3.29) as the result of joining two clusters.

$$d(r,s) = \sqrt{\frac{2.n_r.n_s}{(n_r+n_s)}}\|\bar{x}_r - \bar{x}_s\|^2 \tag{3.29}$$

Where $\bar{x}_r$ and $\bar{x}_s$ are respectively the centroids of clusters r, and s and $n_r$ and $n_s$ the number of elements on each of them.

The number of clusters to be created varies according to the number of elements of the full frame list. It was defined that the average number of elements on each should be approximately 20, as it provides a good separation of different illumination conditions, and the number of clusters being set to achieve that goal. After processing, if the elements of a created cluster greatly exceed that number

(being at least 2.5 times greater) the elements contained in it are sent for additional processing and separation into smaller clusters.

After the clustering process is complete and the clusters created, there is the need to order them and clusters are divided into groups according to the average characteristics of its elements. As mentioned by Grieger [43], the more equatorial maps show very little detail and features when mosaiced using full frames with low incidence angle. For that reason, clusters for maps north of 30°N and south of 50°S are ordered using Figure 3.28 a), while the remaining use Figure 3.28 b).

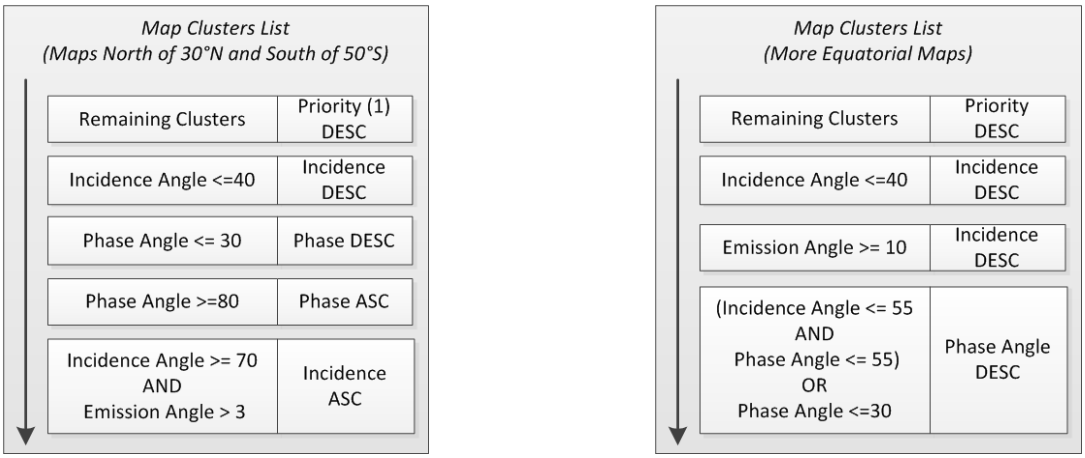


a) b)

Figure 3.28 – a) Map clusters order for maps north of 30°N and south of 50°S. b) Order for the more equatorial, maps.

Each figure shows how groups of clusters are ordered, from top to bottom. On the left side are the characteristics that define each group, on the right how the clusters are ordered inside that group. For the ordering process, the average value of the elements of the clusters is computed and used. The objective of these groups is to isolate clusters with characteristics that may be inadequate for that type of map or create a visually unbalanced map.

Taking into consideration what was described regarding the illumination conditions in chapter 3.3.1.2, maps north of 30°N and south of 50°S focus primarily on full frames with medium to low incidence angle, leaving for last the ones with higher values. Due to the lack of contrast and features, the opposite happens on the more equatorial maps, where the focus lays essentially on full frames with medium-high to high incidence angles.

The remaining clusters, that are not isolated into any of the lower groups, are placed on top of the list and ordered using the average priority value of the elements of the cluster. The full frame priority is described below in chapter 3.3.1.3.1. The only exceptions are the maps covering the poles, which follow Figure 3.28 a) cluster order and where the remaining clusters are ordered by ascending incidence angle instead of the priority. Images on these areas are mostly high incidence full frames and therefore the priority would be placed on these, instead of the lower incidence full frames with more visible features.

After the clusters are ordered, the elements of each cluster are also ordered following the process described in chapter 3.3.1.3.2, that orders the full frames according to their map coverage size.
When all these processes are complete, the ordered clusters and full frames are simply concatenated into a full frames list and sent for mosaicing.

#### 3.3.1.3.1 PRIORITY

It is important to give priority to full frames with certain properties, such as an adequate illumination (not having an incidence angle too low or too high), to create a homogeneous illumination over the map and achieve the best possible resolution,

To do so, let $\emptyset_i$ and $\theta_i$ be the azimuth and zenith angle of the Sun for image $i$. The illumination can then be described by the two dimensional vector of equation (3.30) [43].

$$S_i = \begin{pmatrix} tan\ \theta_i & cos\ \emptyset_i \\ tan\ \theta_i & sin\ \emptyset_i \end{pmatrix} \tag{3.30}$$

It has been suggested by Grieger [43] to multiply the full frame's final priority by the distance to the Moon surface from which the images were taken, but his option has several shortcomings. First, despite allowing for higher resolution full frames to gain higher priority and being projected first, most of these do not mosaic into the best visually mosaiced map and look overexposed, especially at low to medium incidence angles. Since they cover a smaller area there is also the need for more images to be mosaiced, increasing the possibility for divergent illumination conditions and mosaicing imperfections.

Also, as the weighting is only done after the priority is computed, the "lead" illumination does not take into account the coverage. This makes for the possibility of incorrectly selecting the illumination, as is the case when there is a large number of small images (covering a small portion of the AMIE map) and a small number of larger images (that may cover a larger area on the map).

For these reasons, added to the pixel resolution of even the biggest full frame being more than enough for the proposed map pixel resolution, it allows for the opposite solution of giving higher priority to the larger covering images. Therefore, the weighted "lead" illumination direction is then selected as the one that minimizes equation (3.31) for all the $\mathrm{n}$ images of the map.

$$\sum_{\mathrm{i}=1}^{\mathrm{n}} \sqrt{\frac{\|\mathrm{S_i} - \mathrm{S_0}\|}{d}} \tag{3.31}$$

Where $d$ is the distance from the Moon's surface from which the full frame was captured. This equation should select an illumination for which there is the highest number of full frames with similar illumination conditions covering the largest area.
After obtaining this, equation (3.32) attaches an "illumination deviation" to each image $i$.

$$\delta_{\mathrm{i}} = \|\mathrm{S_i} - \mathrm{S_0}\| \tag{3.32}$$

This approach is only applied to maps north of 30°N and south of 50°S as in more equatorial maps the images with lower incidence angle show a small amount of features and low contrast. For these, the homogeneity was sacrificed in favour of a lower sun and equation (3.33) was used instead, with $\alpha_{\mathrm{i}}$ being the angle of incidence of the full frame.

$$\delta_{\mathrm{i}} = \frac{|\tan(\alpha_{\mathrm{i}} - 75°)|}{d} \tag{3.33}$$

#### 3.3.1.3.2 COVERAGE SIZE

Even with the full frame priority being weighted with its size there are still cases of images with a poor contribution to the mosaiced map. More importantly, the mosaicing process can create an unnecessary overlapping effect that affects the visual balance, uses unnecessary images and greatly increases the computation time.

After applying the described process it was found that on some maps the amount of images used on the mosaicing process could be reduced by up to 33%. The processing of each cluster is presented in Figure 3.29 and described below.

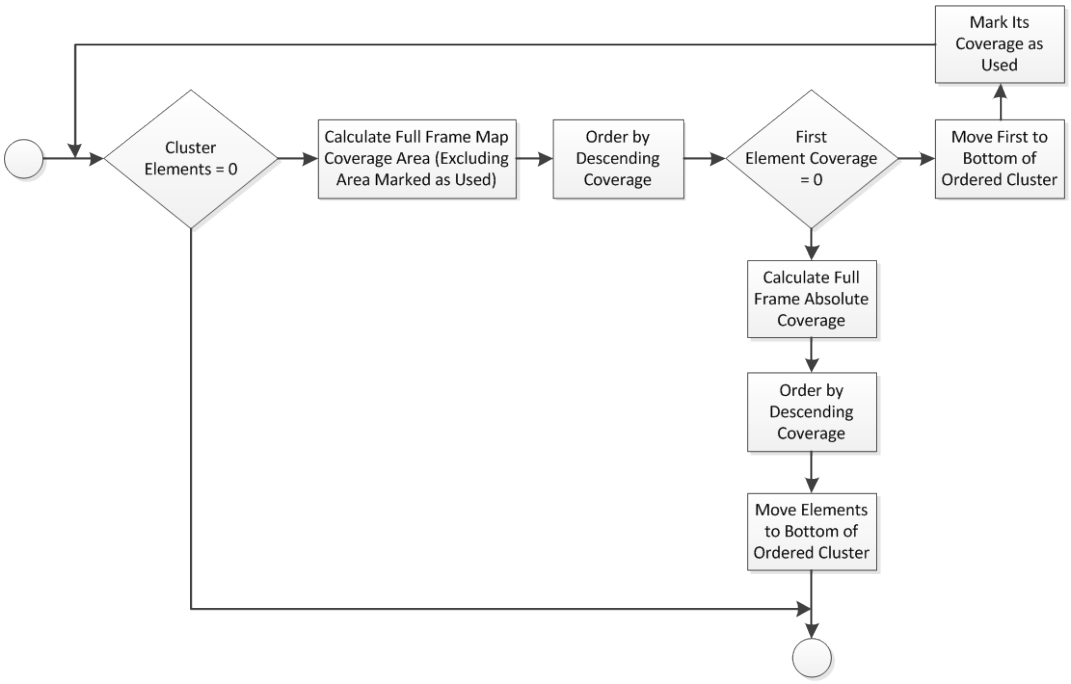


Figure 3.29 - Coverage size ordering process

The full frames coverage area is computed using the full frame corners latitude and longitude coordinates. The one with the larger map coverage is selected, moved to a new ordered cluster and its area marked as used. If the full frame coverage extends beyond the edges of the map its coverage is adjusted to only the area inside it.

The process then iteratively continues, moving the one with more coverage and going down along the list. The exception is that, after the first full frame, is excluded from the full frames coverage the area of the map marked as used from other moved images, as exemplified on Figure 3.30. The full frames projected represent the areas of the map marked as used, the red area represents the coverage of the image being analysed that overlaps it and the white line the coverage that is taken into account for ordering.

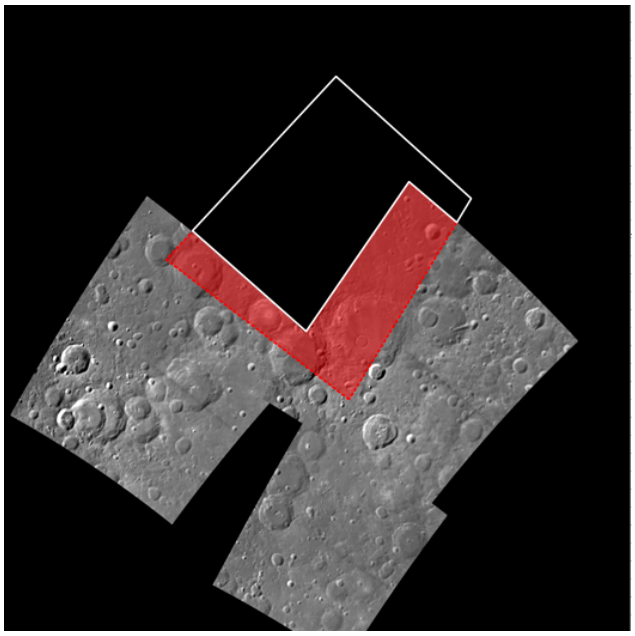

Figure 3.30 - Coverage computation example

Using the corners coordinates as reference points provides an excellent compromise between needed computation and coverage accuracy, but the does not take into account the corrupted band on top of the full frame and the areas that are not projected after the classification on chapter 3.3.1.1. Even though the predicted area coverage takes that into account the same is not possible for the reference points. This may lead to mark areas as used that are not. For that reason, when the remaining images no longer provide additional map coverage they are simply ordered by their overall coverage area and moved to the already ordered cluster, instead of just ignored.

When the process for the first cluster is done, the same is then subsequently done along the others, but now taking into account the areas of the map already marked as used and adding to them as it computes the clusters.
The coverage size ordering minimizes the number of images used to mosaic the map. When it is applied to the whole map full frame list the mosaicing uses the absolute minimum amount of images regardless of priority or image quality. Having it applied only over the created clusters ensures it only orders images who share the same characteristics, not having the drawback of moving bad quality images over good ones just for having larger coverage.

### 3.3.2 Full Frames Projection

The full frames projection is done using a low resolution 120 x 128 geometric grid as mesh warping [44], with the coordinates of the intermediate pixels computed by bi-linear interpolation [45] and forward warping used with distance interpolated splatting [46].

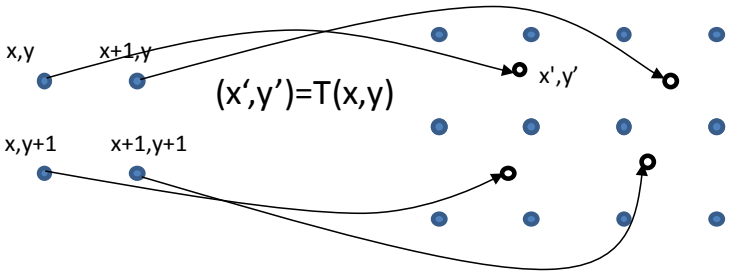


Figure 3.31 - Image forward warping

In the projection, the images coordinates $x, y$ are transposed to the coordinates $x', y'$ following equation (3.34). While $x, y$ coordinates are integers the $x', y'$ transposed coordinates are decimals, which would mean these would be located in the intermediate space between the true pixels location.

$$(x', y') = T(x, y) \tag{3.34}$$

To solve this, each transposed pixel location is transformed to the true pixels integer location using distance interpolated splatting technique, where the pixel value is distributed among the neighbouring pixels. The contribution of each pixel value to the neighbouring ones (equation (3.35)) is obtained by inversely weighting the distance between the transposed location and neighbour true pixel location (equation (3.36)) [47].

$$Cont(p_a, p_b) = V(p_{a,}) * W(p_a, p_b) \tag{3.35}$$

$$W(p_a, p_b) = \frac{1}{1 + K.Dist(p_a, p_b)} \tag{3.36}$$

Where $V(p_a)$ is the transposed pixel value, $Dist(p_a, p_b)$ the distance between transposed location and neighbour true pixel location, given by equation (3.37), and $K$ controls the spread amount among the neighbouring pixels. With $K = 0$ the pixel value is spread with constant amount, as $K$ increases the spread will progressively be lower. In this case for the full frames projection $K = 1$ was used. Equation (3.37) was used for distance computation, instead of the more common square root distance, for its higher computation efficiency while maintaining low quality degradation.

$$Dist(p_a, p_b) = |x_a - x_b| + |y_a - y_b| \tag{3.37}$$

The contribution $Cont(p_a, p_b)$ of all transposed pixels $p_a$ on the true pixels location $p_b$ is accumulated as well as the weights $W(p_a, p_b)$ applied in the process. The transposed full frame will then be the accumulated contribution, normalised by dividing the accumulated weights applied for each pixel.
Initially a neighbourhood of the 4 closest pixels was used for splatting technique but latter was changed to the 16 closest pixels, as it produced a better value distribution on frames that covered larger areas of the map.

## 3.4 MAP BUILDER

A tool designated *Map Builder* was created with two main goals in mind. The first is to provide the user an appropriate interface for the map mosaicing process, allowing the desired map to be selected and following the mosaicing process as it is executed and the images projected. After the process is completed the new map can be edited to correct any undesired, inadequate or unbalanced images. This option is also available by loading previously created maps from the files created during the mosaicing process.

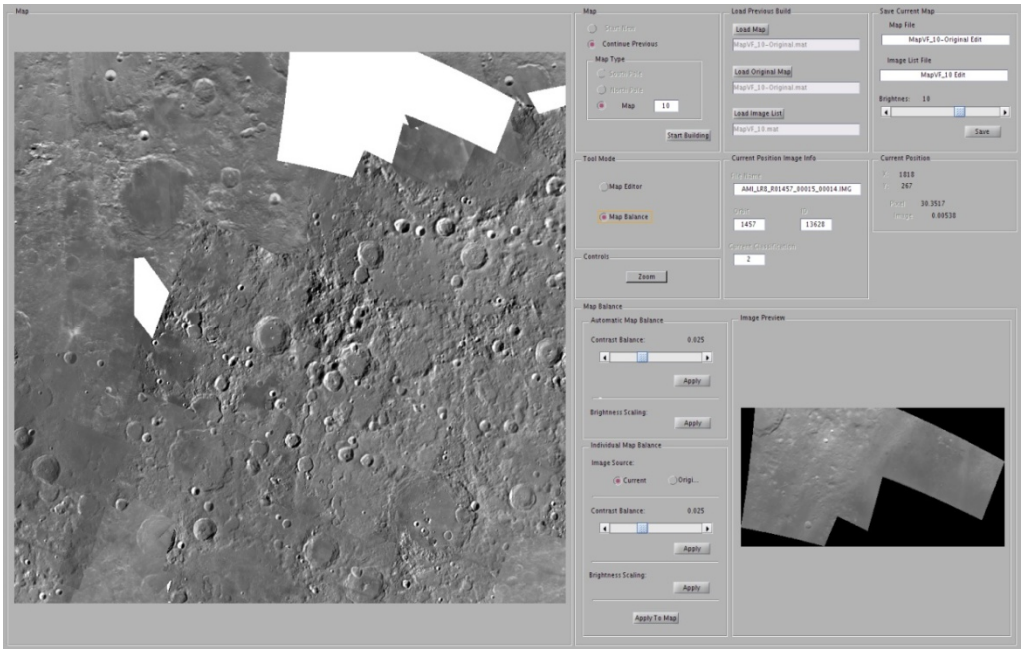


Figure 3.32 - Map Builder in balance mode loaded with AMIE map 10

The brightness scaling effectively reduced the illumination difference between frames but, as described in chapter 3.1.4, in some cases there were still a noticeable brightness difference on mosaiced maps. Figure 3.32 shows an example of one of the worst cases, with the abnormal white full frame image selected and isolated for preview on the lower right corner of the tool.
Additionally, the different incidence angles of the captured frames create images with variable contrast. This contrast instability is not compensated by the brightness scaling creating mosaiced maps with unbalanced contrast.

Therefore, the second goal of the tool is to mitigate these effects and create a more balanced map by implementing the proposed solutions described on chapters 3.4.3 and 3.4.4. Before these solutions can be implemented, each image needs to be isolated and made computational efficient using the segmentation process described on chapter 3.4.2.

### 3.4.1 MAP BUILDER TOOL

The *Map Builder* tool works by selecting whether the map to be worked is based on a previously built map or on a new one, as well as what kind of map it is (north pole, south pole or map 5 to 72). If a previously build map is selected, the tool is loaded with two map files and a file containing the information of which full frame contributed to each pixel.

One of the maps loaded is the one to be built. The other works as a backup map from which the manual map balance (of the *Map Builder* balance mode, described in chapter 0) can load the unaltered images. The backup of the original map can be the same file as the one being worked, but

having it loaded separately allows loading previously unfinished works while always having the unaltered version. If the new map option is chosen all the files are automatically loaded when the mosaicing process is complete.

The tool has two modes, edition mode and balance mode. Alternating between them changes the visible available panels. Edition mode allows the user to replace and modify an image at any point on the map by reprojecting them. Balance mode modifies the brightness and contrast of the already projected images with the goal of obtaining a visually balance map.

The full mosaiced map viewing brightness is adjustable on the *Save Current Map* panel. Clicking on the *Save* button stores the map with the current brightness, allowing the adjustment of the desired brightness for the final AMIE mosaiced maps.

#### 3.4.1.1 EDITION MODE

The edition mode presented in Figure 3.33 starts by clicking to select a point on the map and converting this position to latitude and longitude coordinates. Using these coordinates each full frame belonging to the map is checked for containing them. To do this the four corner coordinates of the full frame image are used to create a polygon that is then used to check if the selected coordinates are inside of this polygon. The frames that contain the selected coordinates are presented to the user in the *Position Image List* of the *Map Builder* edition mode, along with their priority, frame classification and map covering area (in degrees).

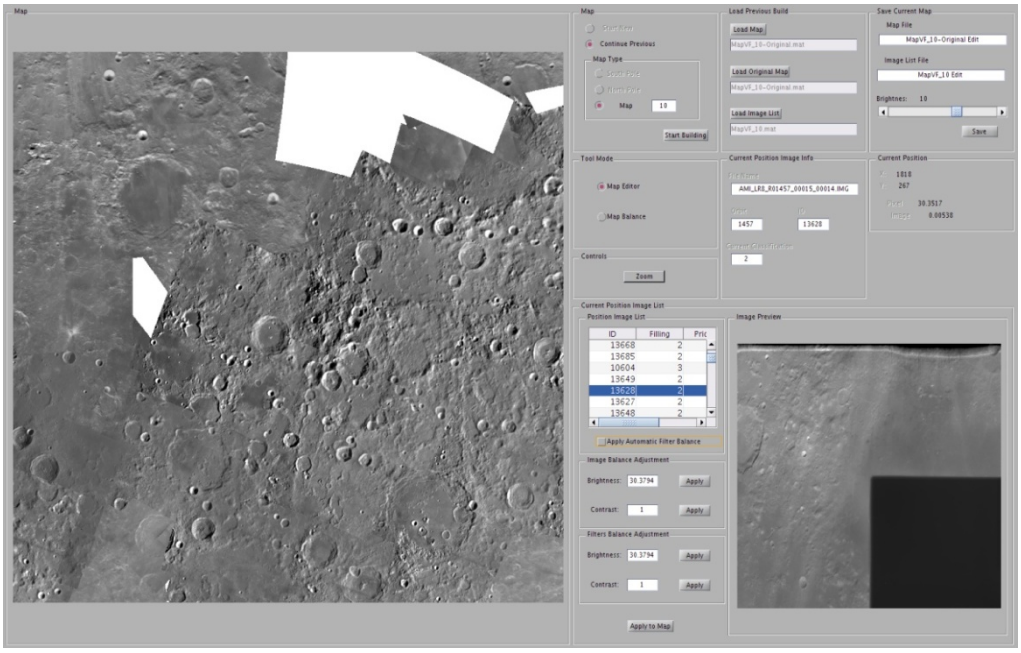


Figure 3.33 - Map Builder in edition mode loaded with AMIE map 10

Selecting a full frame in the previously mentioned the correspondent image is loaded and projected onto the map, replacing the previously existing image in that position. Before doing so, the brightness and contrast differences between filtered and unfiltered areas of the selected full frame can be corrected, as well as the overall contrast and overall brightness. The first contrast adjustment uses the MPOS-DCT algorithm from chapter 3.1.6.2, while the overall contrast uses the adjusted version described on chapter 3.4.4.

#### 3.4.1.2 BALANCE MODE

The *Map Builder* balance mode (Figure 3.32) is divided into automatic balance and individual map balance, both following the process described on Figure 3.34.

Using the automatic contrast balance the user can select the desired estimated contrast balance and have it applied to all the projected images on the map. The contrast balance feature also allows the user to choose whether to balance by just increasing contrast or also by reducing the contrast of those images that considerably exceeds the desired value.

The automatic brightness balance implements the brightness scaling process described on chapter 3.4.3 and applies it over all the images in the map.

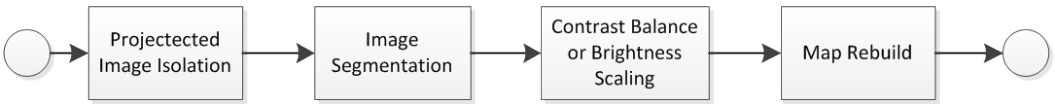


Figure 3.34 – *Map Builder* balance process

By clicking on the map the user can load the information of the image correspondent to the pixel that was clicked, which also includes clicked pixel value, AMIE full frame classification and image estimated contrast. Clicking also enables the manual map balance where a particular image is isolated using the process described in chapter 3.4.2 and the contrast can be adjusted and brightness scaling applied.

Since the contrast adjustment and brightness scaling are a lossy process, and information cannot be recovered, sometimes it is necessary to apply the adjustment over an unaltered isolated image. For that purpose the user can choose the source of the isolated image to be enhanced and applied over the map, either the current map or the original unaltered map.

### 3.4.2 IMAGE SEGMENTATION

During the mosaicing process the information of which full frame contribute to which pixel is stored. That information can be used to easily isolate any projected image of a mosaiced map as in Figure 3.35

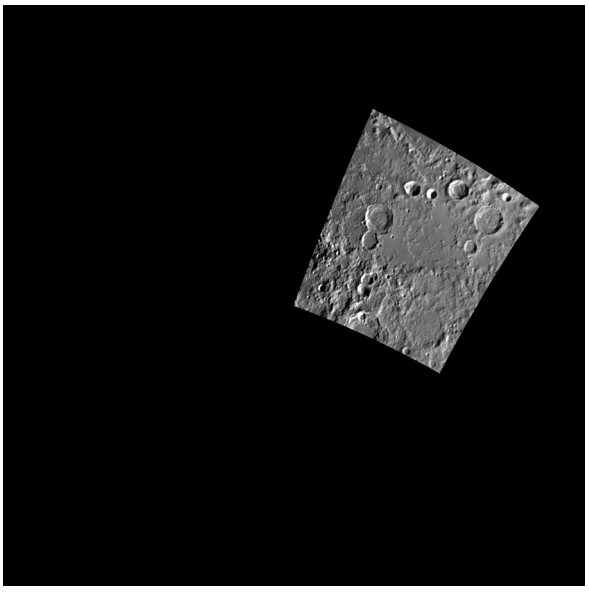

Figure 3.35 - Full frame number 104 from orbit 81 isolated from map 10

A full frame image only covers a small part of the mosaiced map and applying contrast enhancement for map contrast balance over the isolated image from Figure 3.35 would require a large amount of computation. To reduce the amount of computation required the image is segmented, using its horizontal and vertical projections to limit it only to the area covered by the image.

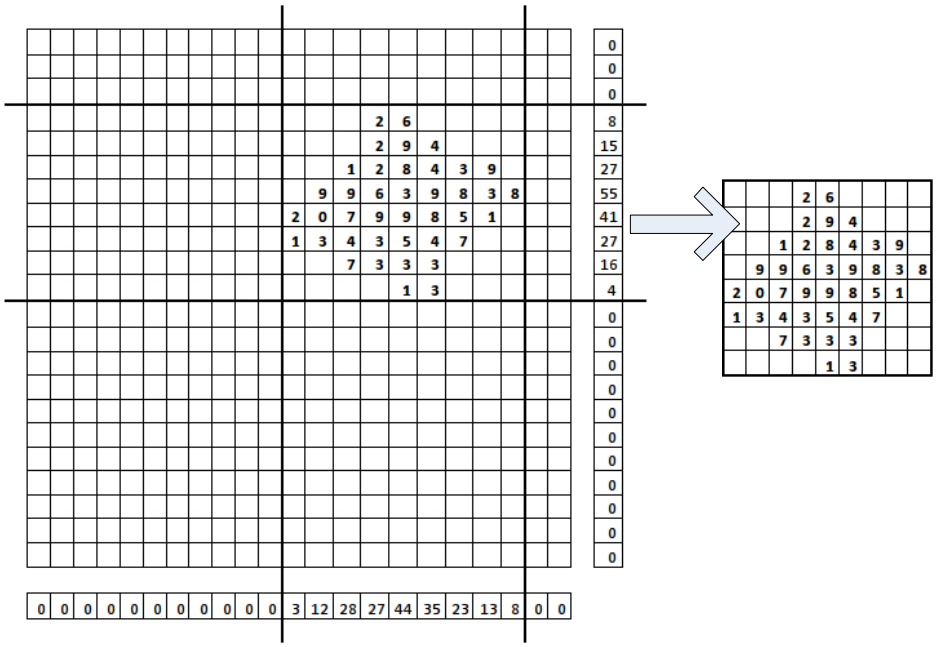


Figure 3.36 - Segmentation process simple example

Since the areas with values are the ones that correspond to the projected full frame the image could basically be considered as a binary image. As Figure 3.36 exemplifies, the process uses the count of the vertical and horizontal projections to isolate the areas where both counts are different than zero value. These areas are then reanalysed for their new counts and subdivided into new reduced areas if necessary. The process is continuously executed until the areas containing the projected image cannot be further reduced.

### 3.4.3 MAP BRIGHTNESS SCALING

The brightness scaling from the Hapke model gives a good brightness balance for most mosaiced maps. However it is not consistent enough to be used by itself on all of the AMIE maps. For those presenting problems with the modelled brightness another empirically designed scaling is applied.

This scaling simply consists of computing the mean value of the isolated image on the map, using only data values that are above a minimum, as presented in equation (3.38). $i_{max}$ and $j_{max}$ are the dimensions of the isolated image and $n_{sum}$ the number of pixels of the isolated image $Img$ that have data values above $minVal$.
Pixels with data values below this are considered pixels on the shadow areas of the terrain, which are therefore are not taken into account for the computed mean. By doing so, the underestimation of the mean value on full frames with large shadow areas and low visible terrain (caused by high incidence angle) is significantly reduced.

$$Mean = \frac{1}{n_{sum}} \times \sum_{i=1}^{i_{max}} \sum_{j=1}^{j_{max}} Img(i,j)\,[Img(i,j) > minVal] \tag{3.38}$$

Examining the full frames data values it was found that these are best viewed when presented on a dynamic range of 0 up to 10 data values. Of these, shadow areas of the full frames tend to contain values below 1 data value.
The exceptions are full frames with extremely elevated incidence angles (equal to or above 85°). These have a higher maximum value and shadow areas with a variable range that cannot excluded by a fixed number. To compute the $minVal$ for these cases an approximation to remaining was done by measuring each individual image maximum value and making $minVal$ equal to 10% of this number. For these cases, the computation of the $minVal$ follows equation (3.39).

$$minVal = \begin{cases} 1, & incidence\ angle < 85° \\ 0.1 \times \max(Img), & incidence\ angle \geq 85° \end{cases} \quad (3.39)$$

Using the computed mean the isolated image is then divided by this value to achieve the brightness balance.

### 3.4.4 MAP CONTRAST SCALING

To compensate for the contrast differences on the mosaiced map a contrast enhancement process was implemented, based on the previously described RSC contrast measure (chapter 3.1.6.1) and the MPOS-DCT contrast enhancement (chapter 0).

The RSC contrast measure is computed as previously described, with the main difference being the cases where the image has too small area for the DOG computation to produce data values. On these cases the Gaussian filters radius are reduced to $r_c = 1$ and $r_s = 2$.
While the segmentation process reduces the image only to the minimal quadrilateral area containing the isolated projected image this projected image doesn't generally have a quadrilateral shape, leaving non-relevant areas. To remove their effect, these are marked as non-interesting and excluded from the contrast measure computation.

The MPOS-DCT has to suffer some minor alterations. First the weighting matrixes for the compensation matrices no longer need the filtered/unfiltered edge protection, that are noticeable as large black stripes on Figure 3.15.
The projected images also have variable width and height, and the block size for the local contrast enhancement should vary accordingly. For the local contrast enhancement it was found that a matrix of 8 by 8 blocks would produce good results and the block size is then adjusted for each projected image. By choosing the 8 by 8 blocks matrix set, the minimal segmented image size that could adequately be used is 64 pixels of width or height. If both width and height fits this minimal requirement the local MPOS-DCT algorithm is used. If either one fall beneath that value the contrast enhancement is done by global DCT adjustment.

The *Map Builder* tool also offers the option to do a full contrast adjustment, reducing the contrast of isolated images that greatly exceeds the desired contrast value. This option takes advantage of the DCT contrast enhancement ability not only to increase but also to reduce the images contrast.

# 4 CONCLUSIONS AND FUTURE WORK

This thesis presents a method for the construction of a Moon atlas, based on the lunar mapping performed by the AMIE instrument on-board of the SMART-1 spacecraft. The process starts from the dataset full frame calibration and proceeds to solutions for an adequate image selection and ordering. This aims to achieve visually balanced maps. The mosaicing and projection of the captured images is the final process in the map creation. A tool with the ability to manage the process, edit and balance the mosaiced maps is also presented as an appropriate interface for the user.

A Moon atlas is always a great source of interest both for the scientific community studying the lunar surface and its composition as for the enthusiasts to whom Earth's natural satellite is a source of wonder. For scientific study it is important not to use image processed maps as a source, as the processing modifies the data. With that in mind, and despite that the focus while building the algorithm was to achieve a visually pleasant atlas, it was also provided that the mosaicing of lunar maps was performed without any additional image processing.

The overall coverage of the atlas is in line with the initial expectations at the beginning of the project. Table 4.1 shows the lunar surface coverage of each of the individual AMIE maps using the dataset. As it can be noted, despite the exclusion of the full frames images considered visually poor, the overall surface coverage can be considered high. After all the processes are concluded and the maps mosaiced, the overall coverage is 97.31%.
While the overall maps coverage has a quite satisfying value, it is also important to mention that in some maps the number of available images in the dataset itself was small, forcing the mosaicing process to use lower quality images containing visible unpleasant features. That was one of the main reasons for the design of a tool that could reduce contrast difference between mosaiced images.

Table 4.1 - AMIE map's images coverage percentage

| Map Index | 1 | 2 | 3 | 4 | 5 | 6 | 7 | 8 | 9 | 10 |
|---|---|---|---|---|---|---|---|---|---|---|
| 1..10 | 100% | 100% | 100% | 100% | 98.95% | 100% | 100% | 98.60% | 100% | 100% |
| 11..20 | 99.724% | 99.82% | 93.15% | 100% | 99.90% | 100% | 97.52% | 98.85% | 99.19% | 95.85% |
| 21..30 | 99.74% | 93.08% | 88.34% | 93.51% | 96.72% | 100% | 100% | 99.37% | 95.23% | 97.89% |
| 31..40 | 99.24% | 96.06% | 99.99% | 98.73% | 82.34% | 98.05% | 91.62% | 99.99% | 100% | 99.68% |
| 41..50 | 96.62% | 98.47% | 99.21% | 97.71% | 99.85% | 98.31% | 77.96% | 96.32% | 89.34% | 100% |
| 51..60 | 100% | 99.92% | 98.19% | 99.41% | 99.57% | 99.52% | 99.96% | 98.10% | 63.56% | 96.97% |
| 61..70 | 98.96% | 100% | 100% | 99.98% | 98.29% | 99.40% | 100% | 99.01% | 100% | 98.64% |
| 71..80 | 72.58% | 98.66% | 99.48% | 99.52% | 100% | 99.91% | 99.98% | 99.89% | 100% | 100% |
| 81..88 | 100% | 100% | 100% | 95.88% | 100% | 100% | 99.98% | 82.83% | | |

Considering the large amount of data available in the AMIE dataset, execution time was also a concern. Processing time for each individual full frame in the early stages (including scattered light enhancement, map image list selection and mosaicing) was close to 80 seconds. Considering that each map has an average of nearly 400 images and the poles at least 3000, that amount of time was not acceptable. This forced the implementation of functions in the most efficient way and the storage in the database of the data resulting from this process (such as the scattered light amount of necessary filter improvement). This way it was possible to reduce processing time in approximately 80%, achieving close to 15 seconds per full frame. Although it is still a considerable execution time, taking into consideration the amount of mathematical analysis required by this process that value can be considered acceptable.

Making a general and critical analysis, this work provides an overall improvement over the initial stage of mosaiced maps, with the improved selection of the images to be mosaiced taking the most important role. One of the most complex problems was to create an adequate way of evaluating the image's quality and to create maps that could take advantage of that while maintaining a homogenous look. This was achieved using the capture illumination conditions, as it was considered to provide a

good indicator about the image visual quality. While there are still a low number of cases which fall beyond the expected illumination pattern, that approach improved the quality of the maps.

To finalize, comparison between Annex A and B provides a preview of the evolution of Moon Atlas, with Annex A containing the first ever complete mosaiced maps and Annex B the final version built with the method presented on this Thesis. As it can be seen, the older versions included several damaged or low quality images that significantly limited the overall quality of the resulting maps. Also, the brightness balance was not able to compensate the capture of full frames in different illumination conditions, leaving the feel that they did not belong together in forming a mosaic. It should be noted that, while the Map Builder tool allows editing the mosaiced maps, the version presented in annex B is a simple one containing only contrast and brightness balancing.

## 4.1 FUTURE WORK

A more direct-to-the-problem approach, that included image enhancement, was taken to address the problem of the scattered light between the filters and the CCD. In this approach a contrast definition was used to measure the current contrast in order to evaluate the necessary enhancement. One of the biggest issues is that there is no definitive contrast definition in literature and a large number of definitions are available. Furthermore, it has to provide an accurate contrast evaluation of images' different areas that might have completely different kind of features. While the chosen definition provides good results for the large part of the dataset, no absolute measure could be achieved.

Also as direct result of the scattered light, in a small number of full frame images there is still a noticeable edge that the implemented solution could not remove. These are essentially caused by severely affected images where this effect led the filters to be underexposed. As this scattered light pattern exhibits a random distribution, with both under and overexposed filter areas, its removal is complex.

A larger percentage than initially expected had at least one part of the full frame considered inadequate for mosaicing. This was in part a result of the different response to light between the different filters and the unfiltered portion of the CCD, and the difficulty to manage the exposure time for all situations between these. Once identified the problematic cases, the classification of each image provides a good starting point for a future research to recover the now unusable parts of the images.

As a future work it could also be interesting to find a method that could adequately fuse different images covering the same lunar area. Space exploration always represented a high scientific investment leading to a limited amount of data results. In the surface mapping, it represents a limited amount of images for a certain area sometimes not all (or any for that matter) with the best quality. In the case of unexplored or highly relevant areas this may have dramatic results. To be able to choose and fuse the best parts of lower quality images and create maps from it can be a very useful solution especially for areas with limited amount of captured images.

# 5 BIBLIOGRAPHY


1. **Bussey, Benjamin.** SMART 1 - Europe at the Moon. *Lunar and Planetary Information Bulletin.* 2005, Vol. 101, pp. 2-3.
2. **Foing, BH, et al.** SMART-1 mission to the Moon: status, first results and goals. *Advances in Space Research.* 2006, Vol. 37, 1, pp. 6-13.
3. **Burchell, MJ, Robin-Williams, R and Foing, BH.** The SMART-1 lunar impact. *Icarus.* 2010, Vol. 207, 1, pp. 28-38.
4. ESA Shares SMART−1 Legacy With The World. *ESA - European Space Agency.* [Online] 18 March 2013. [Cited: 6 June 2013.] http://sci.esa.int/science-e/www/object/index.cfm?fobjectid=47714.
5. **Wilson, Andrew and Marsden, R.** ESA's report to the 36th COSPAR meeting. *ESA Special Publication.* 2006, Vol. 1296.
6. **Estublier, Denis, Saccoccia, Giorgio and Gonzales Del Amo, Jose.** Electric propulsion on SMART-1-a technology milestone. 2007, Vol. 129, pp. 40-46.
7. **Foing, BH, et al.** SMART-1 mission to the moon: Technology and science goals. *Advances in Space Research.* 2003, Vol. 31, 11, pp. 2323-2333.
8. **Josset, J-L, et al.** Science objectives and first results from the SMART-1/AMIE multicolour micro-camera. *Advances in Space Research.* 2006, Vol. 37, 1, pp. 14-20.
9. **Josset, J-L.** *SMART-1 LUNAR/OTHER AMIE 2 EDR RAW DATA EARTH ESCAPE PHASE V1.0, S1-L/X-AMIE-2-EDR-EEP-V1.0.* s.l. : ESA Planetary Science Archive, 2008.
10. —. *SMART-1 LUNAR/OTHER AMIE 2 EDR RAW DATA EXTENDED MISSION V1.0, S1-L/X-AMIE-2-EDR-EP-V1.0.* s.l. : ESA Planetary Science Archive, 2008.
11. —. *SMART-1 LUNAR/OTHER AMIE 2 EDR RAW DATA LUNAR PHASE V1.0, S1-L/X-AMIE-2-EDR-LP-V1.0.* s.l. : ESA Planetary Science Archive, 2008.
12. —. *SMART-1 LUNAR/OTHER AMIE 3 RDR CAL DATA EARTH ESCAPE PHASE V1.0, S1-L/X-AMIE-3-RDR-EEP-V1.0.* s.l. : ESA Planetary Science Archive, 2008.
13. —. *SMART-1 LUNAR/OTHER AMIE 3 RDR CAL DATA EXTENDED MISSION V1.0, S1-L/X-AMIE-3-RDR-EP-V1.0.* s.l. : ESA Planetary Science Archive, 2008.
14. —. *SMART-1 LUNAR/OTHER AMIE 3 RDR CAL DATA LUNAR PHASE V1.0, S1-L/X-AMIE-3-RDR-LP-V1.0.* s.l. : ESA Planetary Science Archive, 2008.
15. **Benestad, R.E.** *Solar Activity and Earth's Climate.* s.l. : Springer/Praxis, 2002. ISBN: 9783540433026 LCCN: 2002067239.
16. **Grayzeck, Ed.** NASA - NSSDC - Spacecraft - Details - Luna 3. [Online] 27 March 2013. [Cited: 8 April 2013.] http://nssdc.gsfc.nasa.gov/nmc/masterCatalog.do?sc=1959-008A.
17. **Grahn, Sven.** The Flight of Luna 3. *Sven's Space Place.* [Online] [Cited: 8 April 2013.] http://www.svengrahn.pp.se/trackind/luna3/Luna3story.html.
18. **Barabashov, N.P., Mikhailov, A.A. and Lipsky, Y.N.** *Atlas of the far side of the moon.* s.l. : Liaison Office, Technical Information Center, 1961. Vol. 1.
19. **Hansen, Thomas P.** *Guide to Lunar Orbiter Photographs.* Langley Research Center, National Aeronautics and Space Administration. Hampton, Virginia : s.n., 1970.
20. **Levin, Ellis, Viele, Donald D and Eldrenkamp, Lowell B.** The Lunar Orbiter Missions to the Moon. 1968, Vol. 218, pp. 58-78.
21. **Williams, David R.** Detailed Information on Lunar Orbiters and Images. *National Space Science Data Center.* [Online] 24 August 2011. [Cited: 8 April 2013.] http://nssdc.gsfc.nasa.gov/planetary/lunar/loinfo.txt.
22. **Bowker, David E and Hughes, J Kenrick.** *Lunar Orbiter photographic atlas of the Moon.* 1971. Vol. 206.
23. **Spudis, Paul D, et al.** The Clementine Mission: Initial Results from lunar mapping. *The Clementine Mission: Initial Results from lunar mapping.* 1994. Vol. 95, p. 24994.
24. **Nozette, Stewart, et al.** The Clementine mission to the Moon: Scientific overview. *The Clementine mission to the Moon: Scientific overview.* s.l. : American Association for the Advancement of Science, 1994. Vol. 266, 5192, pp. 1835-1839.
25. **Sorensen, Trevor C and Spudis, Paul D.** The Clementine mission—A 10-year perspective. *The Clementine mission—A 10-year perspective.* s.l. : Springer, 2005. Vol. 114, 6, pp. 645-668.
26. About Google Moon. *Google Moon.* [Online] Google, 2011. [Cited: 9 April 2013.] http://www.google.com/moon/about.html.
27. **Binder, Alan B.** Lunar Prospector: Overview. 1998, Vol. 281, 5382, pp. 1475-1476.

28. **Grayzeck, Ed.** NASA - NSSDC - Spacecraft - Details - Lunar Prospector. *NASA - NSSDC.* [Online] NASA , 27 March 2013. [Cited: 11 April 2013.] http://nssdc.gsfc.nasa.gov/nmc/masterCatalog.do?sc=1998-001A.
29. **Feldman, WC, et al.** Fluxes of fast and epithermal neutrons from Lunar Prospector: Evidence for water ice at the lunar poles. 1998, Vol. 281, 5382, pp. 1496-1500.
30. **Isbell, Douglas, Morse, David and Rische, Becky.** NO WATER ICE DETECTED FROM LUNAR PROSPECTOR IMPACT - Press Release. *NASA - NSSDC.* [Online] 13 October 1999. [Cited: 11 April 2013.] http://nssdc.gsfc.nasa.gov/planetary/text/lp_pr_19991013.txt.
31. MATLAB - The Language of Technichal Computing. *MathWorks.* [Online] [Cited: 14 July 2013.] http://www.mathworks.com/products/matlab/.
32. **Grieger, B.** *The calibration of AMIE images.* ESA. 2009.
33. **Hapke, Bruce.** *Theory of reflectance and emittance spectroscopy.* s.l. : Cambridge University Press, 2012.
34. **Grieger, B., Koschny, D. and Graf, M.** Towards an AMIE atlas of the Moon. *Towards an AMIE atlas of the Moon.* January 2010.
35. **Peli, Eli.** Contrast in complex images. *JOSA A.* 10, 1990, Vol. 7, pp. 2032-2040.
36. **Simone, Gabriele, Pedersen, Marius and Hardeberg, Jon Yngve.** Measuring perceptual contrast in digital images. 2012, Vol. 23, 3, pp. 491-506.
37. **Tadmor, Y and Tolhurst, DJ.** Calculating the contrasts that retinal ganglion cells and LGN neurones encounter in natural scenes. 2000, Vol. 40, 22, pp. 3145-3157.
38. **Tang, Jinshan, Peli, Eli and Acton, Scott.** Image enhancement using a contrast measure in the compressed domain. 2003, Vol. 10, 10, pp. 289-292.
39. **Kim, Joung-Youn, Kim, Lee-Sup and Hwang, Seung-Ho.** An advanced contrast enhancement using partially overlapped sub-block histogram equalization. 2001, Vol. 11, 4, pp. 475-484.
40. **Allen, Elizabeth and Triantaphillidou, Sophie.** *The Manual of Photography.* s.l. : Focal Press, 2010.
41. **Baalke, Ron.** SPICE - The NASA Planetary Science Division's Ancillary Information System. [Online] 27 June 2013. [Cited: 14 July 2013.] http://naif.jpl.nasa.gov/naif/index.html.
42. **Grieger, B, et al.** Coverage and pointing accuracy of SMART-1/AMIE images. *Lunar Planet. Sci. XXXIX (CD-ROM)(Abstract\# 2221. Lunar \& Planetary Institute, Houston).* 2008.
43. **Grieger, B.** Atlas Information. s.l. : European Space Agency, April 2012.
44. **Wolberg, George.** *Digital image warping.* s.l. : IEEE computer society press Los Alamitos, 1990. Vol. 10662.
45. **Gonzalez, R.C. and Woods, R.E.** *Digital image processing.* s.l. : Pearson/Prentice Hall, 2008. ISBN: 9780131687288 LCCN: 2009289249.
46. **Szeliski, Richard.** *Computer vision: algorithms and applications.* s.l. : Springer, 2010.
47. **Fonseca, JM, et al.** SMARTIC – EXPLORING SMART-1 IMAGES. 2012.
48. **Byers, B.K., National, United States. and Administration, Space.** *Destination moon: a history of the Lunar Orbiter program.* s.l. : National Aeronautics and Space Administration, 1977.

# ANNEX A

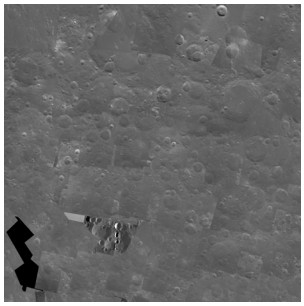

Map 5

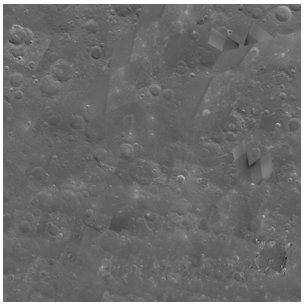

Map 6

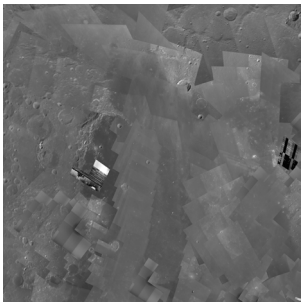

Map 7

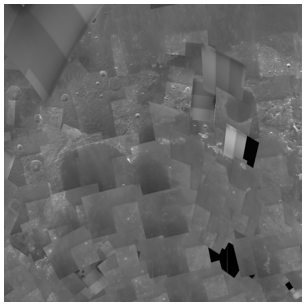

Map 8

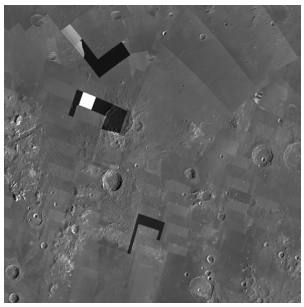

Map 9

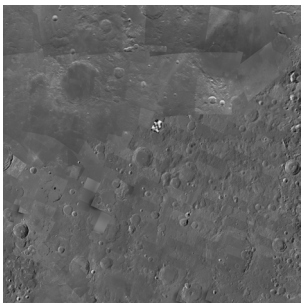

Map 10

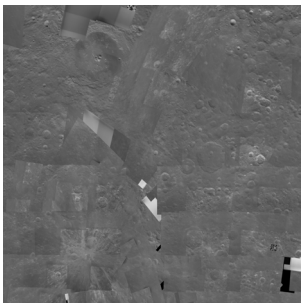

Map 11

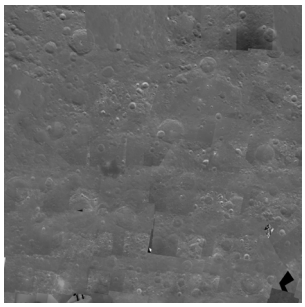

Map 12

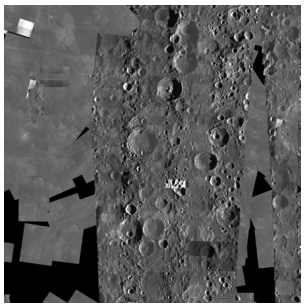

Map 13

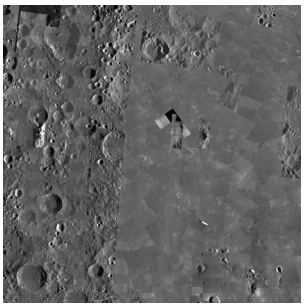

Map 14

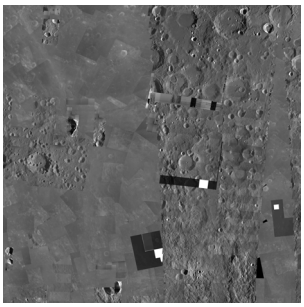

Map 15

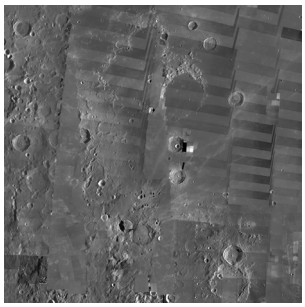

Map 16

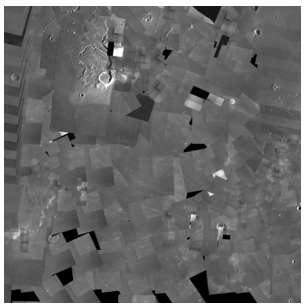

Map 17

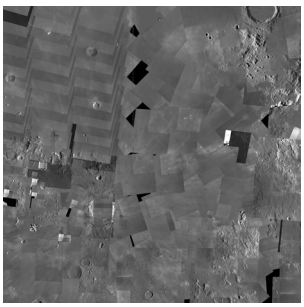

Map 18

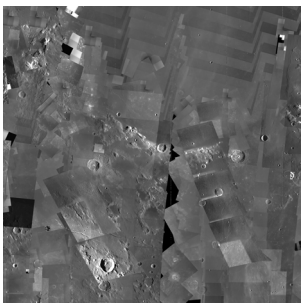

Map 19

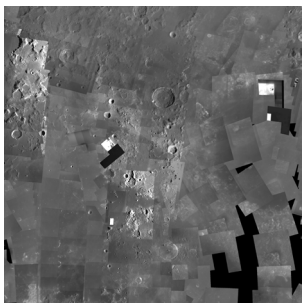

Map 20

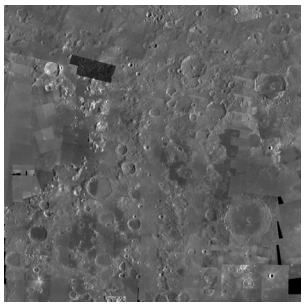

Map 21

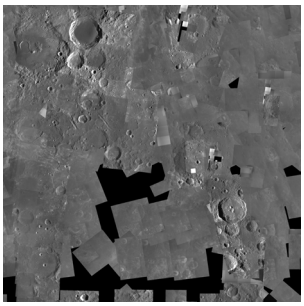

Map 22

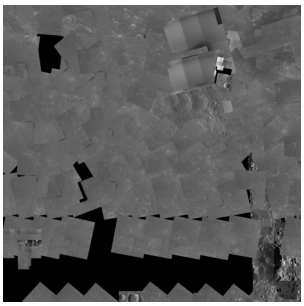

Map 23

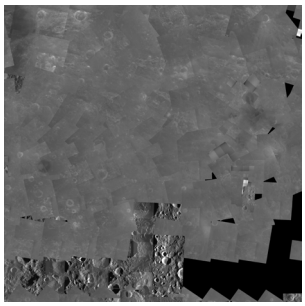

Map 24

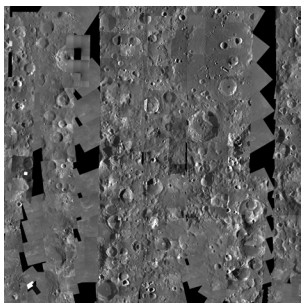

Map 25

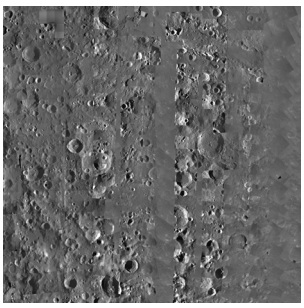

Map 26

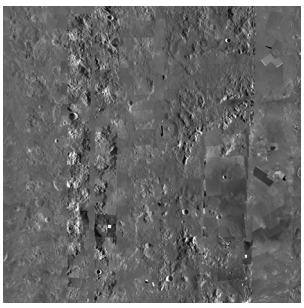

Map 27

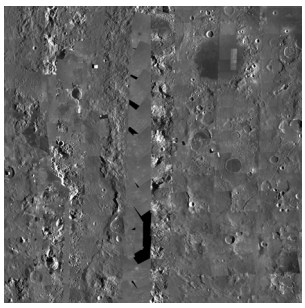

Map 28

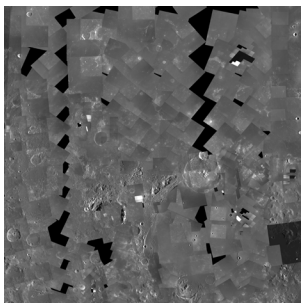

Map 29

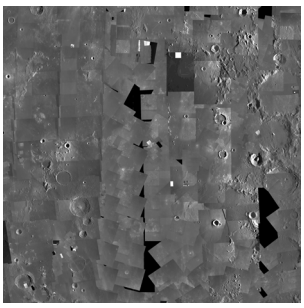

Map 30

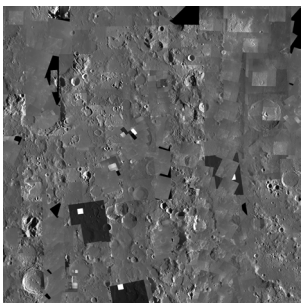

Map 31

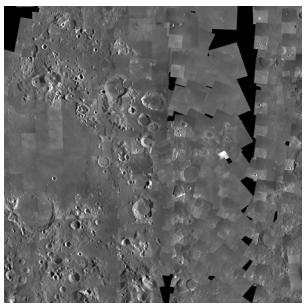

Map 32

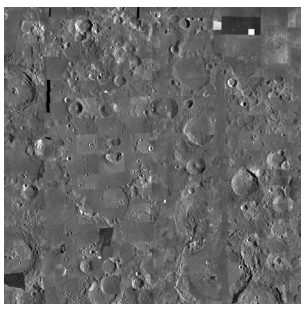

Map 33

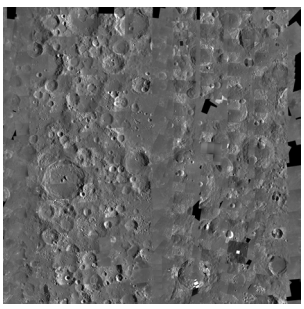

Map 34

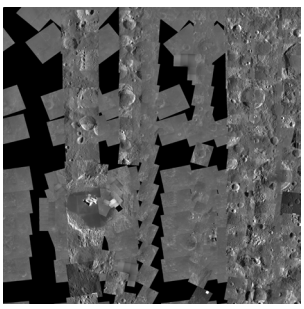

Map 35

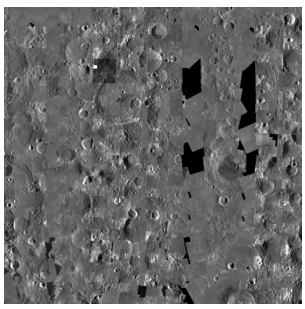

Map 36

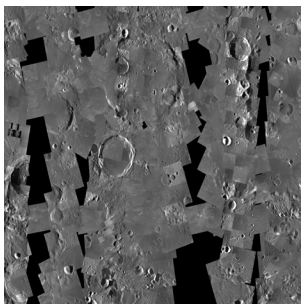

Map 37

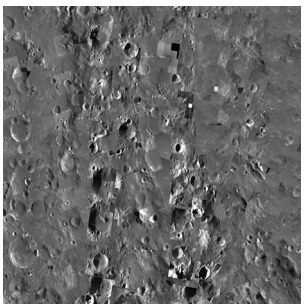

Map 38

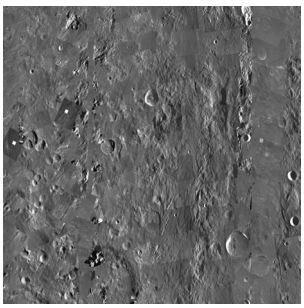

Map 39

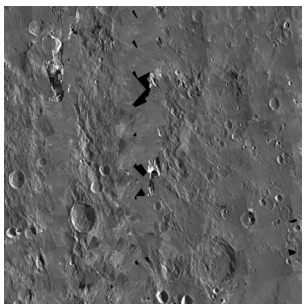

Map 40

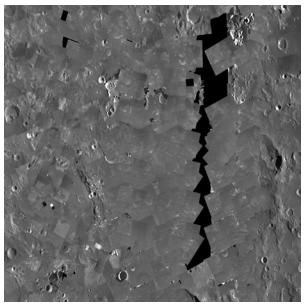

Map 41

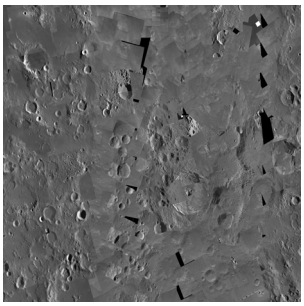

Map 42

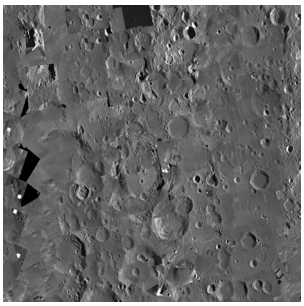

Map 43

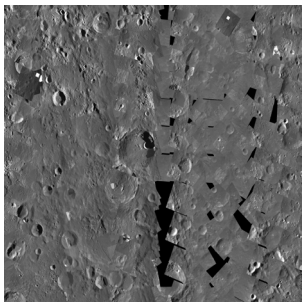

Map 44

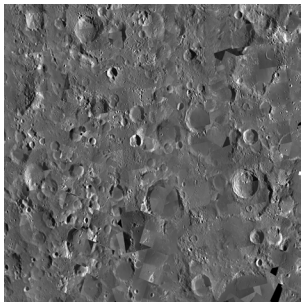

Map 45

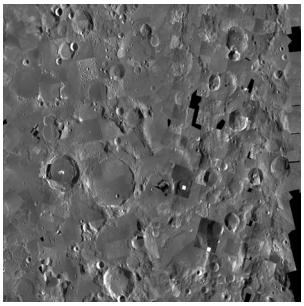

Map 46

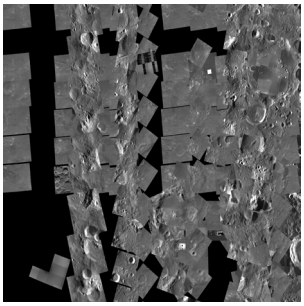

Map 47

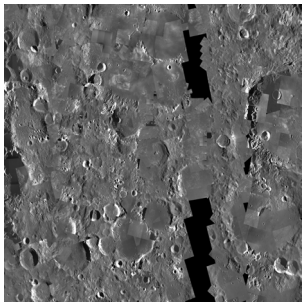

Map 48

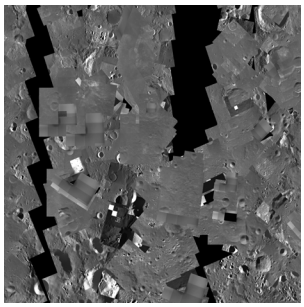

Map 49

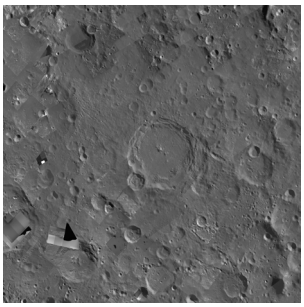

Map 50

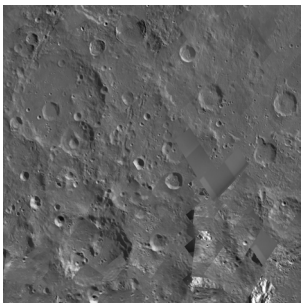

Map 51

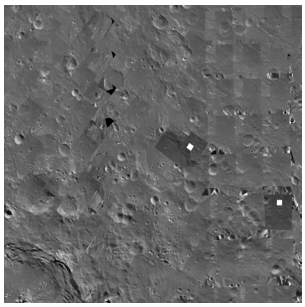

Map 52

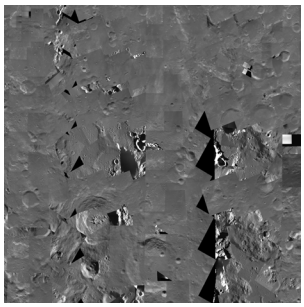

Map 53

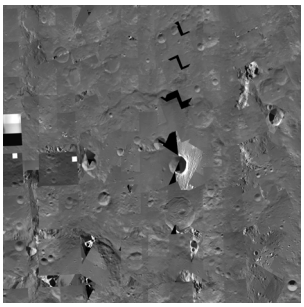

Map 54

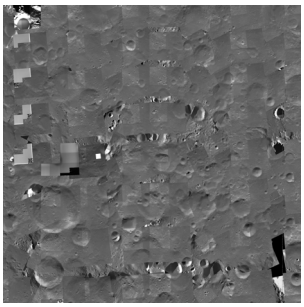

Map 55

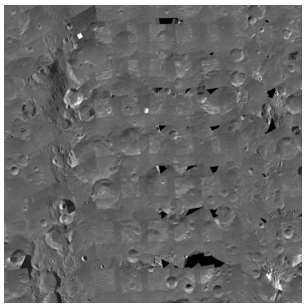

Map 56

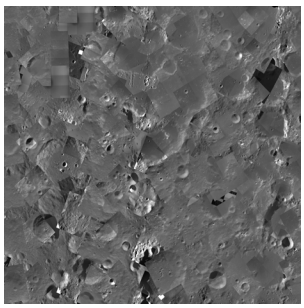

Map 57

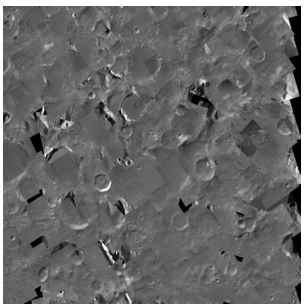

Map 58

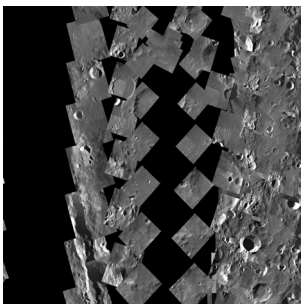

Map 59

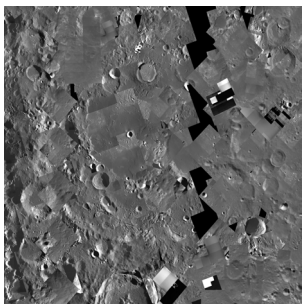

Map 60

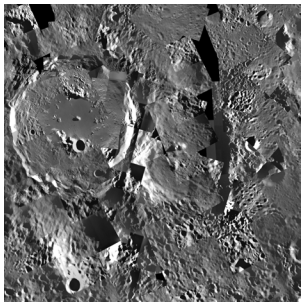

Map 61

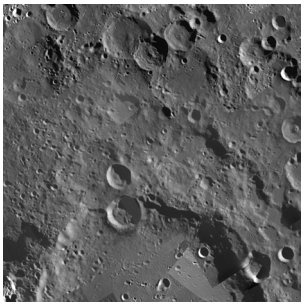

Map 62

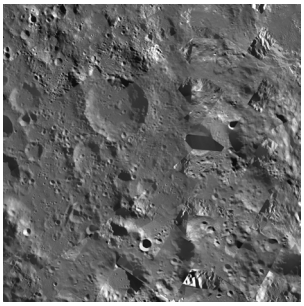

Map 63

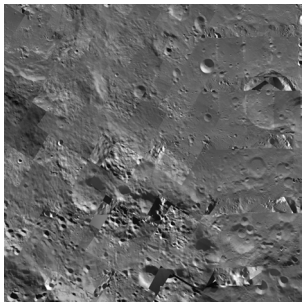

Map 64

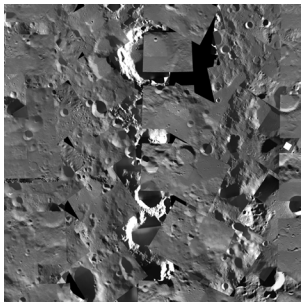

Map 65

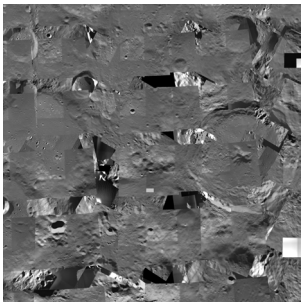

Map 66

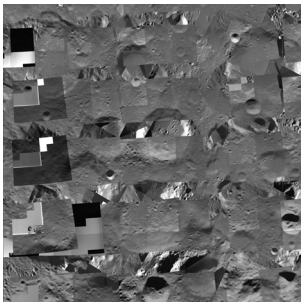

Map 67

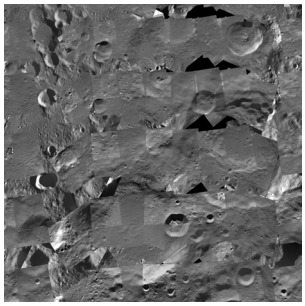

Map 68

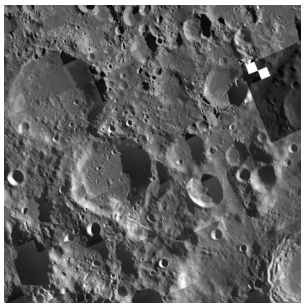

Map 69

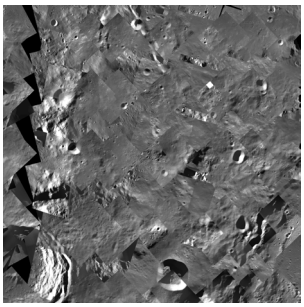

Map 70

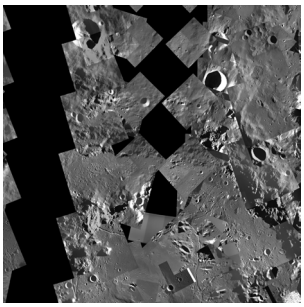

Map 71

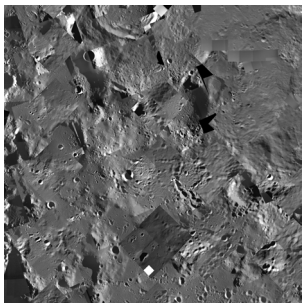

Map 72

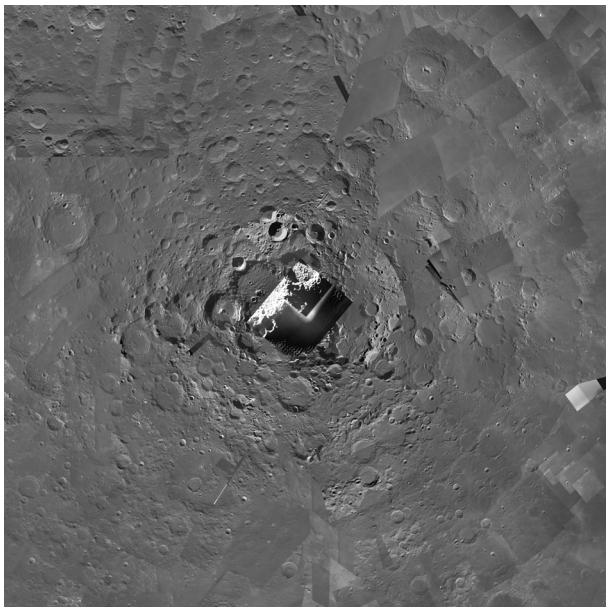

North Pole

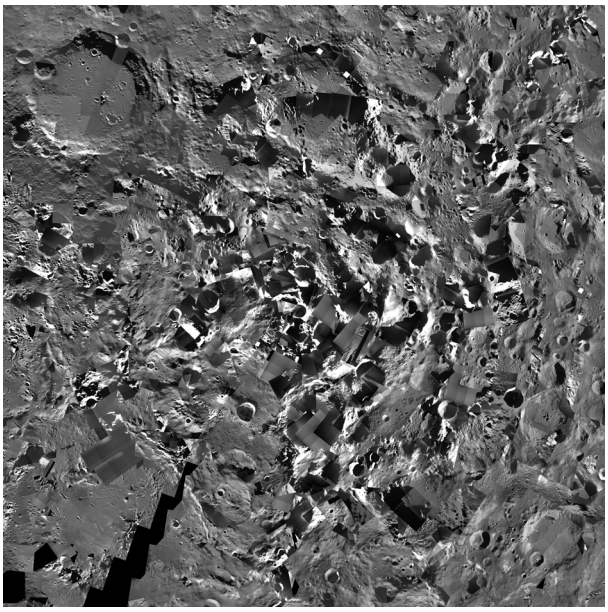

South Pole

# ANNEX B

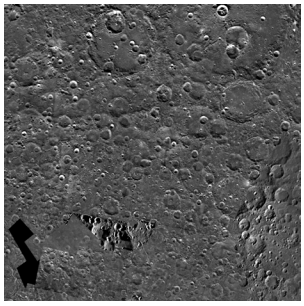

Map 5

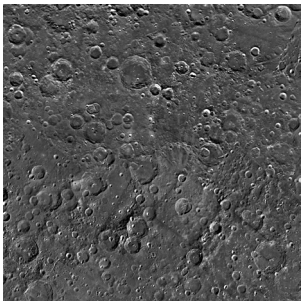

Map 6

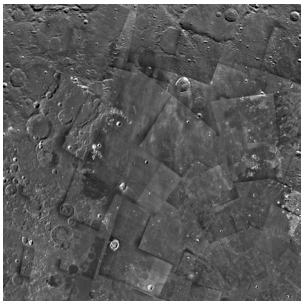

Map 7

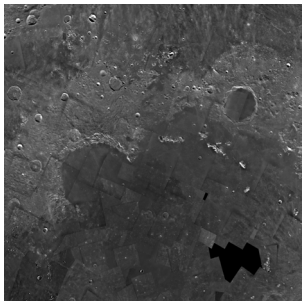

Map 8

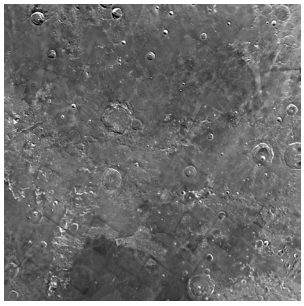

Map 9

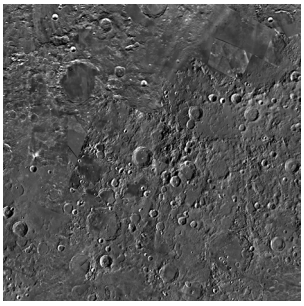

Map 10

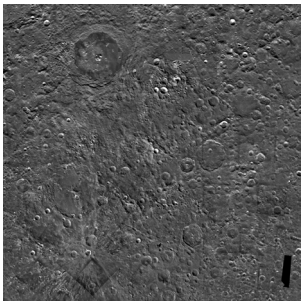

Map 11

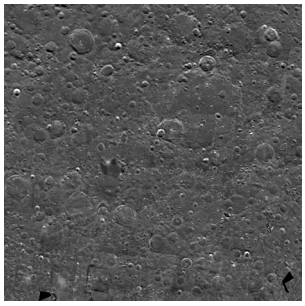

Map 12

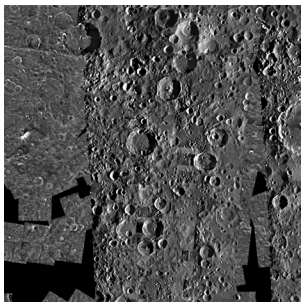

Map 13

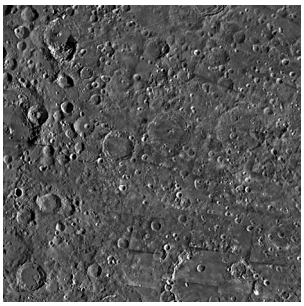

Map 14

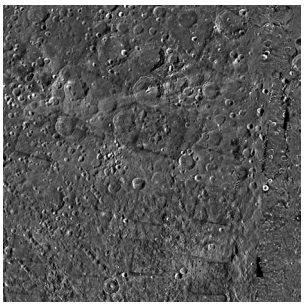

Map 15

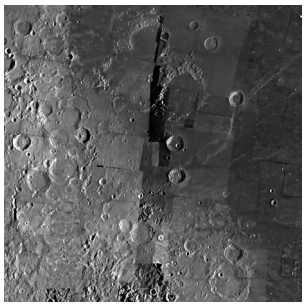

Map 16

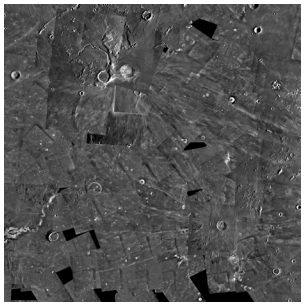

Map 17

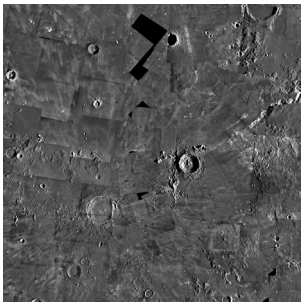

Map 18

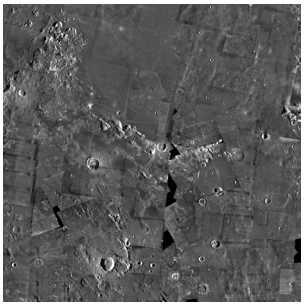

Map 19

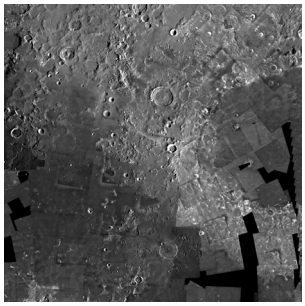

Map 20

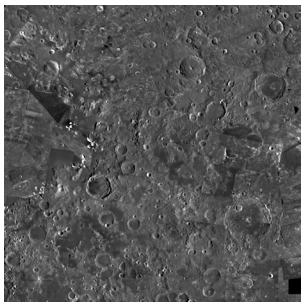

Map 21

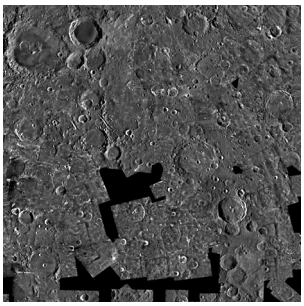

Map 22

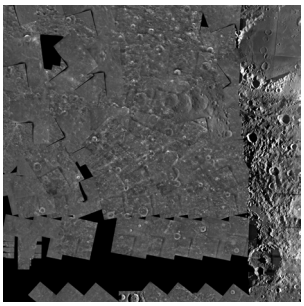

Map 23

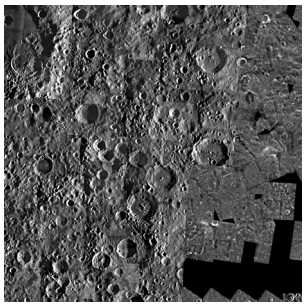

Map 24

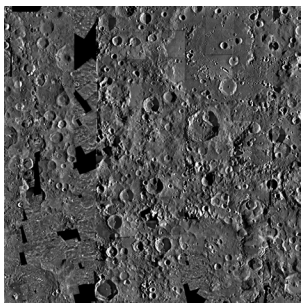

Map 25

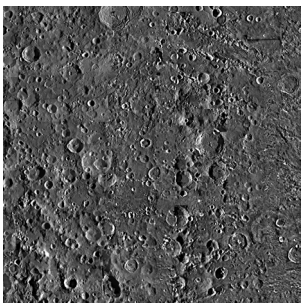

Map 26

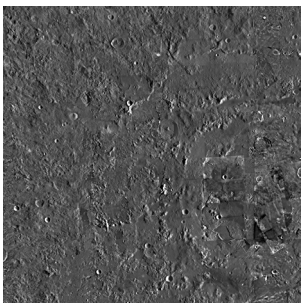

Map 27

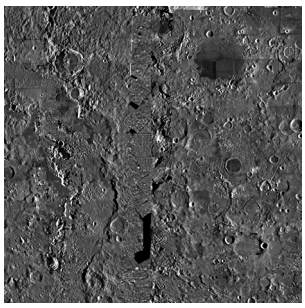

Map 28

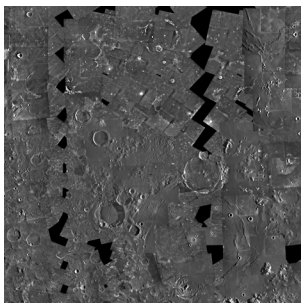

Map 29

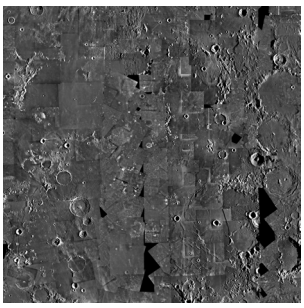

Map 30

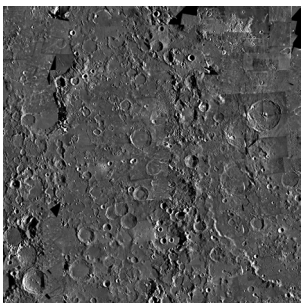

Map 31

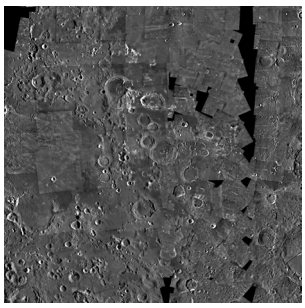

Map 32

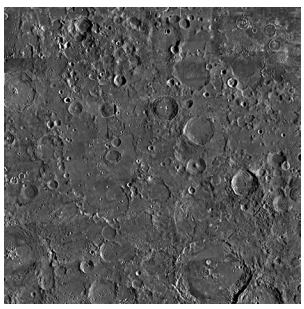

Map 33

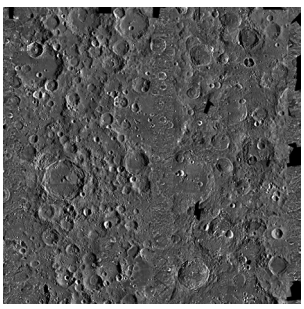

Map 34

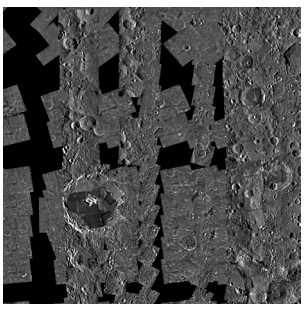

Map 35

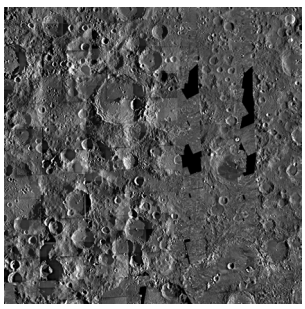

Map 36

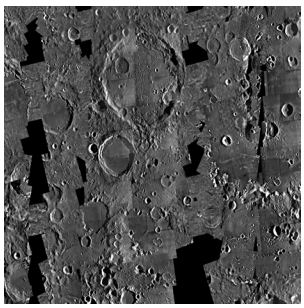

Map 37

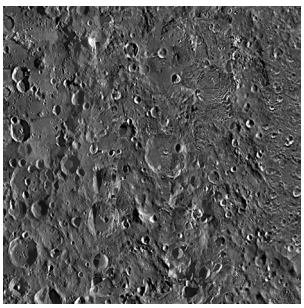

Map 38

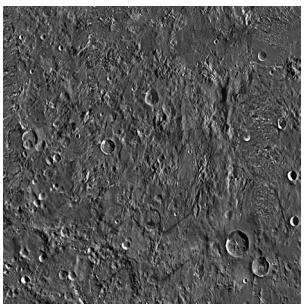

Map 39

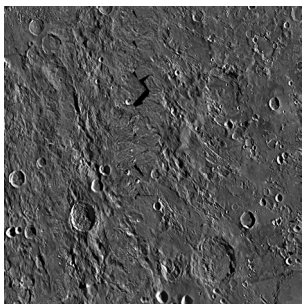

Map 40

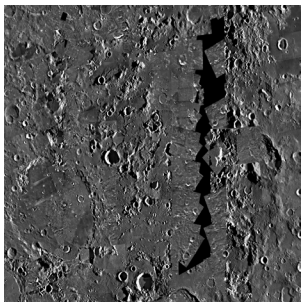

Map 41

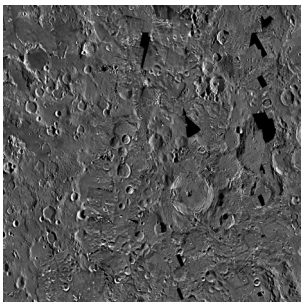

Map 42

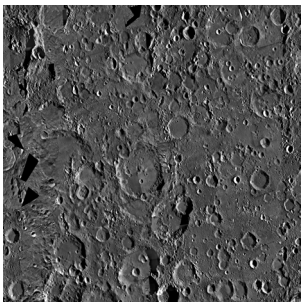

Map 43

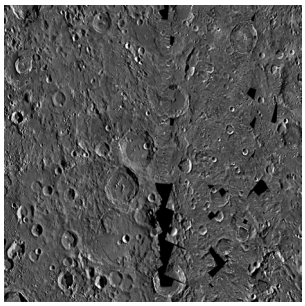

Map 44

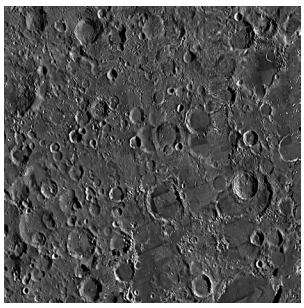

Map 45

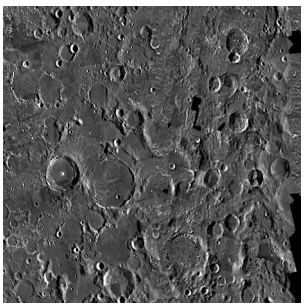

Map 46

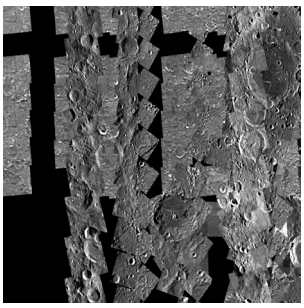

Map 47

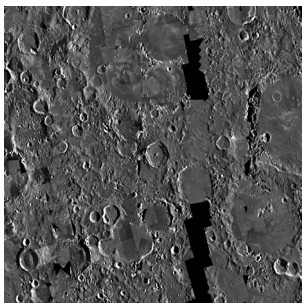

Map 48

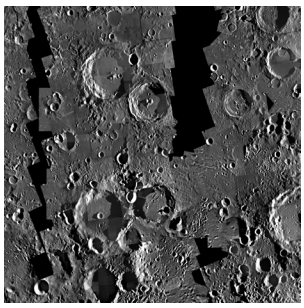

Map 49

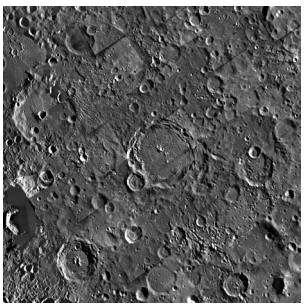

Map 50

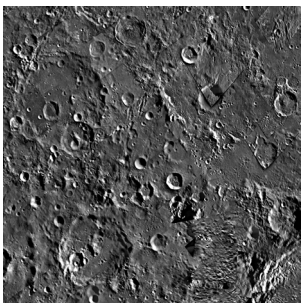

Map 51

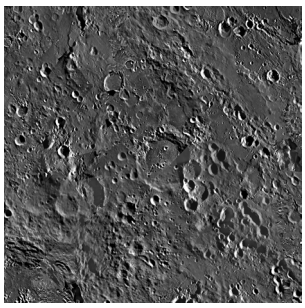

Map 52

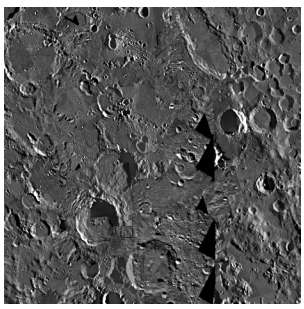

Map 53

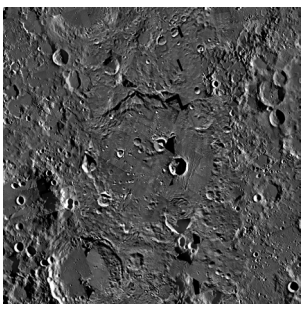

Map 54

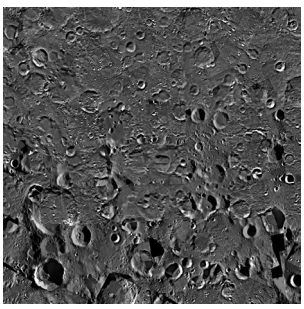

Map 55

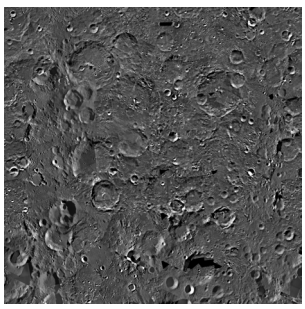

Map 56

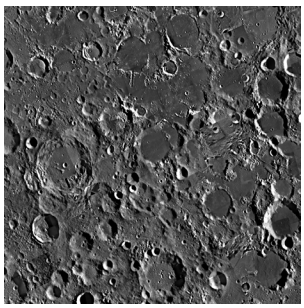

Map 57

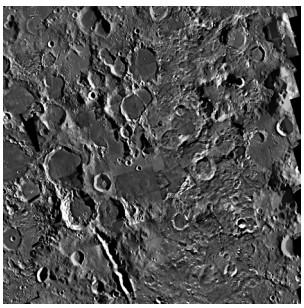

Map 58

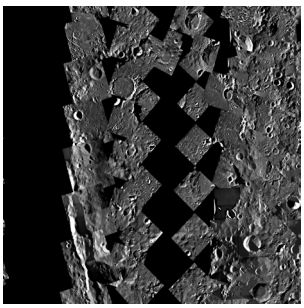

Map 59

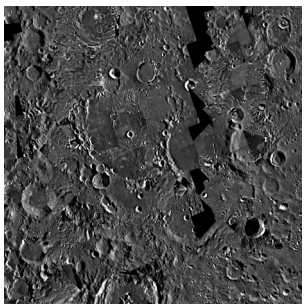

Map 60

Map 61

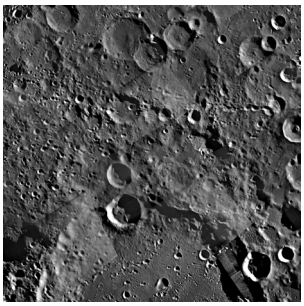

Map 62

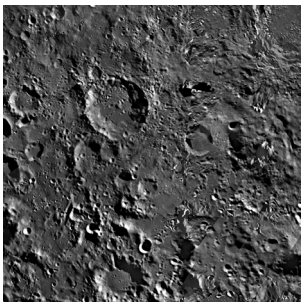

Map 63

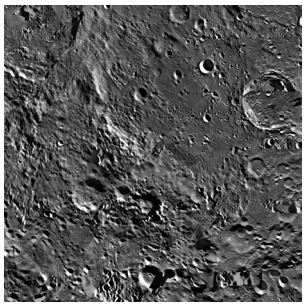

Map 64

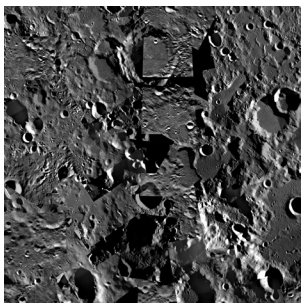

Map 65

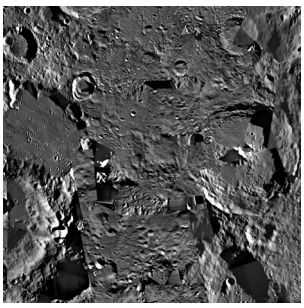

Map 66

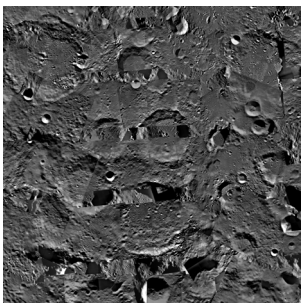

Map 67

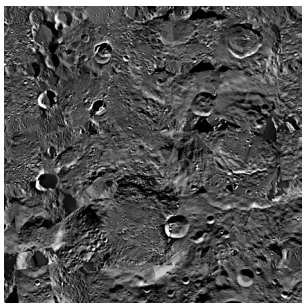

Map 68

Map 69

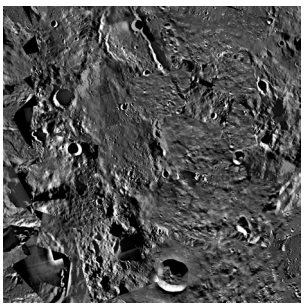

Map 70

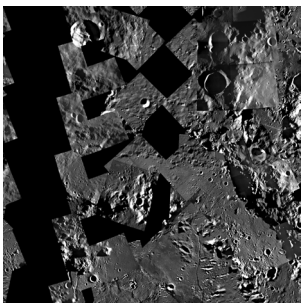

Map 71

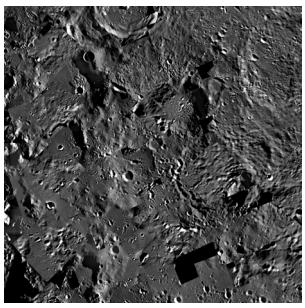

Map 72

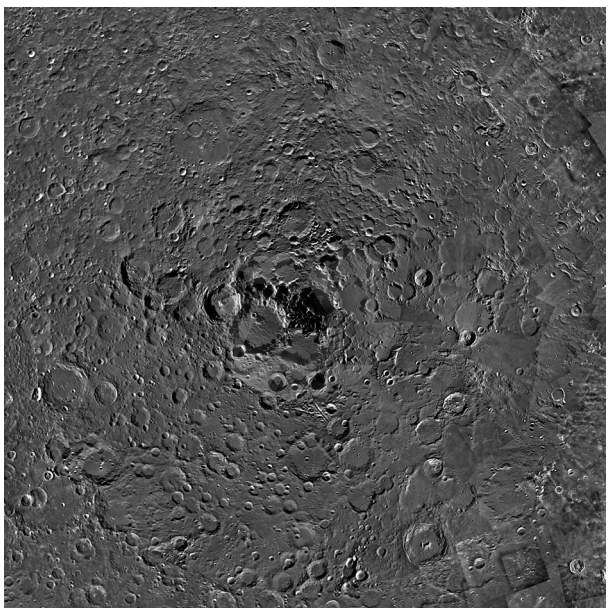

North Pole

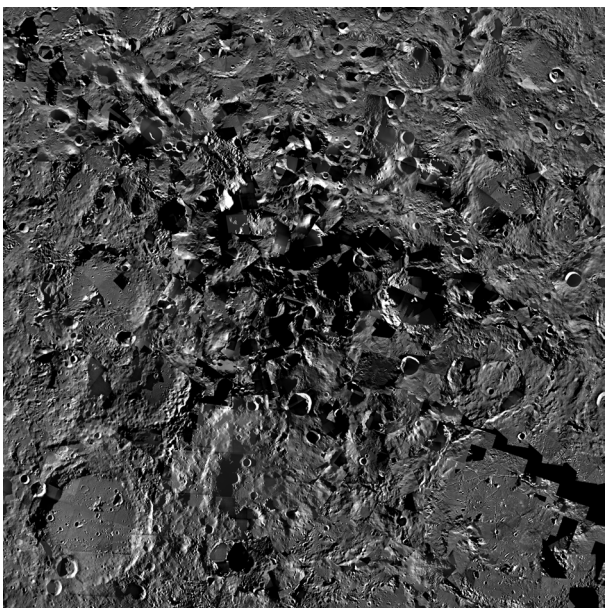

South Pole